Fall 2022

Passive, Self-Healable, Dielectric Elastomers for Structural Health Monitoring

Nicholas Smith
Embry-Riddle Aeronautical University, smithn66@my.erau.edu

Passive, Self-Healable, Dielectric Elastomers for Structural Health Monitoring

By

Nicholas A Smith

A Thesis Submitted to the Faculty of Embry-Riddle Aeronautical University

In Partial Fulfillment of the Requirements for the Degree of

Master of Science in Aerospace Engineering

November 2022

Embry-Riddle Aeronautical University

Daytona Beach, Florida

Passive, Self-Healable, Dielectric Elastomers for Structural Health Monitoring

By

Nicholas A Smith

This Thesis was prepared under the direction of the candidate's Thesis Committee Chair, Dr. Daewon Kim, Department of Aerospace Engineering, and has been approved by the members of the Thesis Committee. It was submitted to the Office of the Senior Vice President for Academic Affairs and Provost, and was accepted in the partial fulfillment of the requirements for the Degree of Master of Science in Aerospace Engineering.

THESIS COMMITTEE

Chair, Dr. Daewon Kim	Member, Dr. Sirish Namilae
Co-Chair, Dr. Foram Madiyar	
Graduate Program Coordinator, Dr. Hever Moncayo	Date
Dean of the College of Engineering, Dr. James W. Gregory	Date
Associate Provost of Academic Support, Dr. Christopher Grant	Date

To my fiancé Kaylie, my better half. To my dogs Louie and Bear, the best friends I will ever have.

ACKNOWLEDGEMENTS

Funding for this project was provided by Florida Space Grant Consortium.

Thank you to my fiance Kaylie, who always lifts my spirits when I am feeling down. You have often given me the push I needed to continue my work and succeed througout graduate school.

Thank you to my advisors Dr. Kim and Dr. Madiyar for often advising me on the best path forward as I completed this research. Their advice has been vital throughout this process, in assuring this research is completed to the highest possible quality. Additionally, thank you for sparking my interest in this topic during the Smart Materials class. Thank you to Dr. Namilae for agreeing to be a member of my committee, and for providing a very positive academic experience in the classroom.

Thank you to my research group for their commaradery and vital input throughout the process, often making suggestions which allowed me to excel. Thank you Scott Bender, Stanislav Sikulskyi, Taylor Stark, Nicholas Reed, Risikesh Srinivasaraghavan Govindarajan, Zefu Ren, Katelyn Branaman, Jackson Schuler, Giovanna Chioro, Sahil Ghate, and John Veracka. An additional thank you to John Veracka, who wrote the grant which funded the purchase of the materials needed to complete the research, before I became involved.

Thank you to my wonderful parents, Julie May, Ph.D., and Randel Smith. M.D. Thank you to my siblings, Brady Smith, Avery Smith, Canon Rogers, and Lily Rogers. I love you all.

ABSTRACT

NASA maintains the ability to track a large majority of objects in Earth's orbit, however lack the ability to track objects smaller than five centimeters in diameter. These untrackable objects represent a significant danger to inflatable structures. This work seeks to synthesize and fabricate a self-healable, passive, dielectric elastomer impact sensor for structural health monitoring on inflatable space structures subject to impact by micrometeoroids and orbital debris. In a setting in which impact repairs can be extremely costly, the implementation of such a technology would not only alert personnel of such an event but would also serve to decrease the cost and time of repairs. This investigation synthesizes an intrinsically self-healing poly(dimethylsiloxane) via a supra-molecular network of multi-strength hydrogen bonds. The modified poly(dimethylsiloxane) network must be effective in harsh environments, particularly extremely low temperatures, as well as retain the dielectric properties of poly(dimethylsiloxane). Self-healing efficiency, stretchability and flexibility are also desirable properties to attain. Integration of the manufactured sensor arrays around a layer of woven ceramic fiber with conductive fabric electrodes, hypervelocity impact testing, and self-healing efficiency tests are performed and confirm the sensors capabilities. The performed tests demonstrate a measurable change in capacitance associated with impact damage and location. Success is represented by passive operation and the penetrated sensors' ability to self-repair without compromising the sensors impact detection capabilities.

TABLE OF CONTENTS`

LIST OF FIGURES

NOMENCLATURE

MMOD	Micrometeoroids and orbital debris
DE	Dielectric elastomer
N	Number of Impacts
F	Flux
A_e	Area of exposure
t	Time
SGA	Soft goods assembly
PVDF	Polyvinylidene fluoride
μ	Micro
C	Capacitance
pF	Picofarads
ε_0	Permittivity of free space
ε_r	Relative permittivity
A	Area of electrode
d	Distance between electrodes
V	Voltage
η	Self-healing efficiency
E	Young's Modulus
σ	Stress
γ	Strain
PDMS	Polydimethylsiloxane
MPU	4,4'-Methylenediphenyl diisocyanate
IU	Isophorone diisocyanate
SS	Disulfide
PEDOT:PSS	Poly(3,4-thylenedioxythiophene) polystyrene sulfonate
UDRI	University of Dayton Research Institute

1 Introduction

This work focuses on synthesizing a self-healable dielectric elastomer, to be evaluated as options for a passive dielectric elastomer (DE) sensor, which may later be integrated into the soft-goods assembly of an inflatable space structure. This research is towards the goal of detecting impacts due to micrometeoroids and orbital debris (MMOD) too small to be tracked by NASA. Ideally the sensor will monitor impacts of MMOD, determine debris size, impact velocity, and depth. Lastly it will utilize the self-healing properties of the synthesized elastomer to repair damage to the sensor from impact penetration.

1.1 Micrometeoroids and Orbital Debris

Environmental hazards such as extreme thermal fluctuation and exposure to micrometeoroids and orbital debris pose a significant threat to space structures [1]. Micrometeoroids are distant comets and asteroids that have found themselves passing nearby or within Earth orbit [2]. According to the National Aeronautics and Space Administration (NASA), "Orbital debris is any human-made object in orbit about the Earth that no longer serves a useful function. Such debris includes nonfunctional spacecraft, abandoned launch vehicle stages, mission-related debris, and fragmentation debris [3]." NASA estimates almost 100 trillion pieces of MMOD in low earth orbit (LEO) travelling at average speeds of 20 km/s and 8.7km/s for micrometeoroids and orbital debris, respectively [1]. According to NASA, "Orbital debris is the number one threat to spacecraft, satellites, and astronauts [4]." The administration has also added, "In fact, millimeter-sized orbital debris represents the highest mission-ending risk to most robotic spacecraft operating in low Earth orbit [3]."

The Department of Defense is capable of accurately tracking space debris in Earth orbit larger than 10cm in diameter. However, NASA lacks the ability to track MMOD smaller than 5cm in diameter [3]. Along with their small size, MMOD are described by their flux [4], the cumulative

number of MMOD to pass through a given area per year [5]. Based upon the work of Kessler and Cour-Palais, using the observed flux of MMOD, models have been developed to determine the size of space debris [1]. Even though the flux decreases substantially as particle size decreases to 1cm in diameter and lower, smaller debris still possess a considerable risk to space structures due to their high velocities, particularly depressurization and structural failure [5]. Given NASA's Handbook for Designing MMOD Protection, the number of impacts, N, can be determined mathematically with the cumulative flux, F (number/m^2-year), exposed are, A (m^2), and time exposed to MMOD flux, t (years), as shown in equation 1 below [5].

$$N = \sum_{i=1}^{n} (FAt)_i \tag{1}$$

As small debris can cause failures such as these, NASA requires, relative to the structure's lifecycle, that habitable space structures be developed to comply with catastrophic penetration probability requirements [5]. Furthermore, given the space industry's growth, it is only logical that space habitats must be designed for more extended service periods and with a greater internal volume, which will of course mean a greater probability of damage due to MMOD impacts. With this increase in risk, implementing an integrated structural health monitoring system is crucial for ensuring the safety of space structures and astronauts.

1.2 Inflatable Space Structures

Volume and structural mass play a vital part in mission cost when developing a spacecraft or cis-lunar architecture [6]. After NASA introduced the TransHub in the 1990s, inflatables have become a promising area of interest [6]. This has led to considerable advancements in space structures and the development of inflatable space structures by implementing a soft goods

assembly (SGA) system. This remains true, as NASA is currently heavily invested into inflatable habitat research through its NextSTEP partnerships [6].

The consideration of inflatable structures arose due to their ability to maximize the operational surface area [6]. Inflatable space structures are designed as multi-dimensional pressure vessels with exterior walls consisting of the aforementioned SGA, aluminum bulkheads, and a rigid core [7]. As shown below in Figure 1.1, the standard SGA setup includes an exterior atomic oxygen shield, multi-layered insulation (MLI), MMOD shielding, a structural restraint layer, and a series of redundant bladders [8].

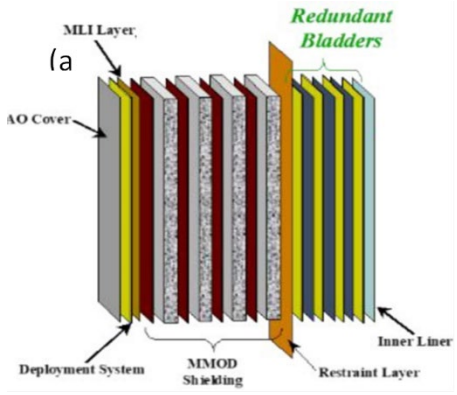

Figure 1.1 A common SGA Layer Assembly [8]

Using this system, deployable structures can be used to greatly reduce mass and stowed volume, allowing for mission cost reductions, or more room for cargo and instrumentation. Following operation, inflatables can be deflated, reducing cargo volume, for a return to Earth for deconstruction. These structures can also easily be incorporated into existing space habitats or other small vehicles [9]. The SGAs of modern inflatables have shown more remarkable performance in MMOD protection in comparison to rigid aluminum sheet protection [5]. Bigelow Aerospace is currently developing an inflatable habitat as a scientific research replacement for

NASA's Destiny module, called the B330 [10]. By comparison, the B330 inflatable will significantly increase the MMOD impact and radiation resistance, as well as the mass-to-volume ratio by over 50 percent [10-12].

This SGA MMOD protection system has been utilized in multiple inflatable structures, including NASA's TransHub, the Bigelow Expandable Activity Module (BEAM), and the Goodyear Aerospace D-21 inflatable airlock. This protection consists of three layers of woven Nextel Fabric separated by open-cell foam with a Kevlar restraint layer [5]. NASA describes the SGA configuration as a Triple Stuffed Whipple Shield with a Kevlar restraint layer. Through hyper velocity impact testing, the protection layer has been shown to stop a 1.7 cm diameter aluminum projectile traveling at 7km/s [5]. In 2016, BEAM became the first human-related inflatable structure attached to the International Space Station (ISS) [9], shown below in Figure 1.2.2 [13]. Following the implementation of BEAM, NASA has increased the technology readiness level of habitable inflatable structures to 9 [9], the highest possible value, meaning it is an existing system, flight proven through a successful mission [14].

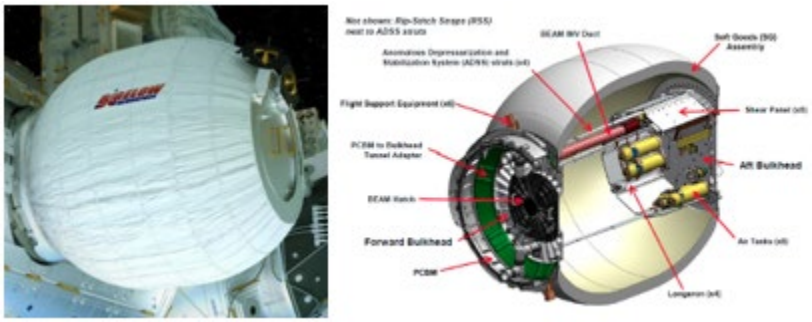

Figure 1.2 BEAM deployed on the ISS (left) and BEAM configuration design (right) [13,9].

With such a rating, it is clear that inflatable space structures will play a vital role in current and future missions as NASA continues with programs such as Artemis and the development of

Gateway. As the immense growth in inflatable space structures continues, research and development of MMOD sensors have increased in recent years.

2 Review of the Relevant Literature

Herein, topics relevant to inflatable space structure MMOD detection are discussed. The current state of the art will first be discussed. This will be followed by a review of parallel-plate capacitance sensors and how dielectric elastomers play a role in this technology. Next, a thorough review of self-healing technology will be given. Finally, the information will be summarized before the following chapter.

2.1 MMOD Detection: Current State of the Art

One method for MMOD detection is applying a thin piezoelectric blanket. This method has shown a 100% accuracy detection rate but is connected to a central electronics module through the pressure hull [5]. A different impact detection method utilizes a distributed impact detection system that implements piezoelectric accelerometers connected to the interior of the SGA [15]. This technology locates the position of the impact and operates by wirelessly using batteries but cannot detect impact depth [15]. MMOD detection has also been explored using a fiber optic micrometeoroid impact sensor. First developed as a method to measure particle flux for solar sails, this sensor was later successfully woven into Kevlar fabric to detect MMOD [5]. The main fault in the technology was that current supporting equipment and electrical interfaces are very heavy, and it is difficult to accurately measure debris size unless many sensors are used [5].

In 2011, a MMOD impact detection sensor was developed using a polyimide dielectric layer with copper electrodes as a capacitance sensor [16]. This sensor was able to measure the impact size and depth, but during hypervelocity testing, the sensor was occasionally shorted, which indicated failure due to penetration [16]. While the demonstrated sensor was flexible, polyimide and copper are not stretchable, which could lead to a risk of damage during inflation and deflation of the structure. In 2019 at ERAU, a previous study funded by SBIR demonstrated a flexible nanocomposite sheet for impact detection. The sensor utilized resistance as its method for

detecting impacts and the severity of the damage [17]. Its downside is due to resistance sensors being non-ideal as a measurements can only be taken periodically due to large energy needs for real-time, in-flight analysis [17].

Previously in 2015, NASA developed and demonstrated an in-situ method of measuring MMOD impact size and velocity, named Debris Resistive/Acoustic Grid Orbital Navy-NASA Sensor (DRAGONS). The device used acoustic polyvinylidene fluoride (PVDF) sensors alongside 25 μm Kapton films coated with resistive lines [18]. When subjected to hypervelocity testing before implementation, the sensor was able to determine the impact size and velocity of the projectile. However, when demonstrations took place aboard the ISS in 2018, the system was only able to determine impact location [18,19].

2.2 Parallel-Plate Capacitance Sensing

All In this work, the sensing method employed is via parallel-plate capacitance. The following subsections give a thorough review of the governing principles, relevant literature, and materials which can be employed to utilize this technology.

2.2.1 Parallel-Plate Capacitors

Capacitors are devices in which a charge is stored [20]. One form of capacitors is the parallel-plate capacitor [20]. This is possible without any material between the parallel plates; however, this would require massive capacitors for a given application. The capacitance may be largely increased with the inclusion of a dielectric material between the plates, usually an elastomer [21,22]. Shown below in the governing equation 2 for the determination of capacitance in a parallel-plate capacitor is given:

$$C = \varepsilon_0 \varepsilon_r \frac{A}{d} \tag{2}$$

Here, the capacitance, C, is determined by multiplying the vacuum permittivity, ε_0, the relative permittivity of the dielectric elastomer, ε_r, and the ratio of electrode area, A, to the distance between electrodes, d [22]. Upon examination of this governing equation, it can easily be seen that a reduction in electrode area will result in a capacitance decrease, whereas a reduction in the distance between electrodes will result in a capacitance increase. This will become important in the following chapter. The general structure of a parallel-plate capacitance sensor is shown below in Figure 2.1.

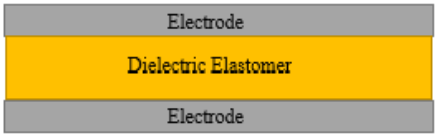

Figure 2.1. Generic parallel-plate capacitance sensor using dielectric elastomer.

As mentioned above, dielectric materials can play an important role within this governing equation. The following subsection will detail dielectric materials in general.

2.2.2 Dielectric Elastomers in Sensors

With applications in structural health monitoring, healthcare, and robotics, Soft DE sensors are a rapidly growing technology [23]. Dielectric elastomers belong within a subsection of electroactive polymers [22]. These materials possess an electromechanical relation, in which mechanical inputs will cause an electroactive response and vice versa [22]. In other words, pressure and strain can be determined through capacitance changes. Until a capacitance change is detected, this effect allows DE sensors to operate in a passive, low-power state [23]. Examples of dielectric elastomers include polydimethylsiloxane (PDMS) [22,24,25], other silicones, acrylonitrile butadiene rubbers, olefinic polymers, polyurethanes, latex rubbers, as well as styrenic and

fluorinated copolymers [22,25]. In flexible sensing devices, due to commercial availability and high performance, silicone and acrylate rubbers are often used, such as VHB, PDMS, and Ecoflex [22].

DE sensors are fabricated by sandwiching a dielectric elastomer between two electrode layers. This combination then exhibits electromechanical efficiency, allowing for high sensitivity to strain and static forces [26]. In addition to high sensitivity, dielectric elastomer sensors may offer advantages such as flexibility, stretchability, and low modulus when measuring force or deformation [22]. This is of great benefit, given that the intended use of soft DE sensor within this work is onboard inflatable space structures, which must be folded, expanded, and folded again as normal procedure. The sensitivity of DE sensors may be further improved via three methods [22]. Sensitivity may be improved by chemical design [27], a difficult task, through use of a conductive filler within the elastomer [28], and by including inorganic, high permittivity particles [29] such as fiberglass fabric [30]. However, one quality of interest concerning dielectric elastomers is recent advancements in their use as self-healing materials. This quality will be explored further in the following section.

2.3 Self-Healing Materials

All living organisms share one trait, the ability to self-repair wounds. Inspired by this trait, researchers have been attempting to replicate this ability through material science research. This ability may provide added longevity to structural health monitoring systems. Materials with the ability to self-heal can be achieved in two ways, extrinsically and intrinsically [31].

Extrinsically healing materials rely on external stimuli, usually dispersed throughout the material. This is typically done with micro-capsules or capillary tubes [31]. Upon damage to the material, either the micro-capsules or capillary tubes are exposed to stimuli such as moisture in the air, or the material itself. Upon exposure to this stimulus, a reaction occurs in which the healing

agent within the capsules or tubes fills in and repairs the damage. As a result of this mechanism, localized healing is limited to single healing cycle [30], as the healing agents in the damaged region are now thoroughly utilized. Extrinsic healing mechanisms are typically used in polymers [31] such as epoxy resins [32], a subclassification of polymers referred to as thermosets.

Intrinsically healing materials rely on interactions within the material matrix itself. Often, this is through reversible bonds within a supramolecular network [24] which interact with each other to repair the damaged area of material [31]. This may be achieved in several ways, particularly hydrogen bonds, pi-pi stacking, van der Waals forces, dipole-dipole interactions, ionic interactions, disulfide metathesis, and metal-ligand coordination [31,33]. This mechanism of healing allows for the same area to be damaged and healed multiple times, imparting a great advantage over extrinsic mechanisms. Intrinsic mechanisms are most often achieved through the use of elastomers [31]. The elastomers employed are typically silicones [34], polyurethanes [35], and other rubbers [36]. One such elastomer which has shown success in the utilization of the intrinsic self-healing mechanism is PDMS. While also showing stability over a wide range of temperatures, an added benefit given the application of this research, autonomous self-healing may be achieved by incorporating multi-strength hydrogen bonds [24] during synthesis of the material.

To determine the effectiveness of self-healing materials and mechanisms, researchers often look to the self-healing efficiency of the material or mechanism in question. The efficiency of a self-healable material, η, a percentage, has been defined in various ways throughout relevant literature. The self-healing efficiency is the ratio of a material property after healing to the material property of a pristine sample [24,33,35-39]. These material properties are Young's Modulus [37], E, maximum tensile strength [38,39], σ_{max}, and strain at break [24,33], γ_{max}. Healing times vary within literature [24,33,38] from 1-2 hours, 6-12 hours, and 24-48 hours, depending on application

requirements. The respective equations 3-5 used to determine the self-healing efficiency are shown below for η_E, $\eta_{\sigma_{max}}$, and $\eta_{\gamma_{max}}$:

$$\eta = \frac{E_{Healed}}{E_{Pristine}} \times 100 \tag{3}$$

$$\eta = \frac{\sigma_{max_{Healed}}}{\sigma_{max_{Pristine}}} \times 100 \tag{4}$$

$$\eta = \frac{\gamma_{max_{Healed}}}{\gamma_{max_{Pristine}}} \times 100 \tag{5}$$

This work believes that all permutations of self-healing efficiency should be considered when evaluating the quality of a self-healable material. Next, intrinsic self-healing achieved via the aforementioned hydrogen bonds must be explored more thoroughly.

2.3.1 Hydrogen Bonding Mechanism of Self-Healing

Within the last 15 years, self-healing mechanisms which employ hydrogen bonding have garnered much attention within the communities studying this biologically inspired phenomenon. This is due to their high healing efficiency, adjustable mechanical properties, rapid healing speed, and chemical structures [40]. As previously mentioned, self-healing elastomers usually achieve their goals through reversible interactions, rupture, and re-formation, of various chemical bonds [40]. According to Xie *et al.* [40], hydrogen bonding represents one such reversible interaction which is extremely versatile due to its tunable strength, dynamic nature, and responsiveness to external stimuli. Furthermore, the ease of synthesis, availability of starting materials and functional derivatives [40] make this method of self-healing extremely promising for practical applications. One such example of this is shown on the following page in Figure 2.2.

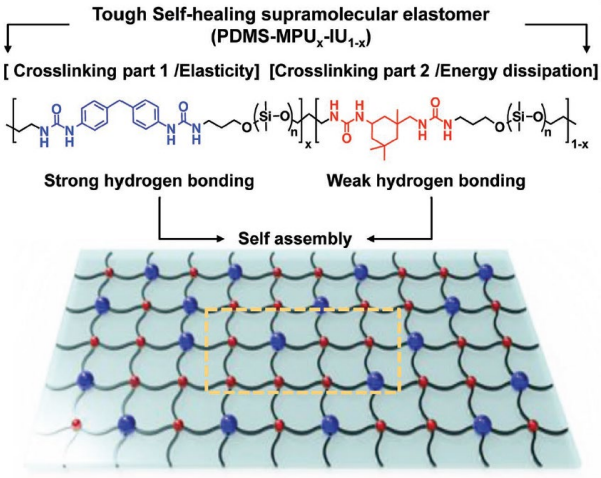

Figure 2.2 Supramolecular elastomer network for self-healing achieved through hydrogen bonding [24].

The structure of hydrogen bonds can be described simply as a proton donor and a proton acceptor [40]. Though the strength of single hydrogen bond is around one tenth of the strength of a covalent bond, 40 kJ/mol and ~400 kJ/mol respectively, it is still stronger than simple van der Waals forces [40]. Because of this, hydrogen bonding is fairly weak molecular interaction in the traditional sense [40]. Interestingly, the strength of hydrogen bonds varies in a wide range from highly dynamic to quasi-covalent [40], warranting further exploration within the scientific community. This quality has led researchers to use the highly dynamic hydrogen bonding to synthesize polymers of low Young's modulus and mechanical strength but possessing excellent healing properties [40]. The use of strong, quasi-covalent, hydrogen bonds has allowed researchers to synthesize polymers with much stronger mechanical properties and high Young's moduli, but at the cost of weaker healing properties [40].

Xie *et al.* [40] asserts that the strength of connection and self-healing properties may be balanced through multiple hydrogen bonding types and has garnered extensive attention within the scientific community. This may be achieved through double, triple, quadruple, linear, and zig-zag

arrays within supramolecules [40]. These options can affect properties such as mechanical strength, extensibility, toughness, and healing efficiency [40]. The system of multiple hydrogen bonds may find themselves positioned within polymers in the main chain, chain ends, side chains, and in the ends of hyperbranched structures [40]. According to Xie *et al.* [40], "The position of multiple hydrogen-bonding units will determine the density of H-bond cross-linking that will further affect the final properties of the materials. For the multiple hydrogen-bonding polymers, the mechanical performances of the final polymers are strongly dependent on the amounts of multiple hydrogen-bonding units or the density of cross linking."

Bao *et al.* [41] recently developed several supramolecular self-healing materials via incorporation of hydrogen bonding agents within the main chain of their chosen polymers [40, 41]. The researchers found that the introduction of hydrogen bonding within the main chain affected the microphase morphology, mechanical properties, and healing efficiency in their material, achieving mechanical performance and healing efficiency balance [40,41]. This material exhibited 93% recovery in tensile strength and toughness when healed at 80°C for 24 hours [41]. Fu et al. claims to have achieved a novel strategy of multiple hydrogen bonds within the main chain to realize fast and effective room temperature healing under ambient and harsh conditions [40,42]. Their work used thiourea moieties were used within a polyurea network to form multistrength, dynamic reversible hydrogen bonds [40,42].

Regarding hydrogen bonding units as chain ends, Xie *et al.* [40] state that this method can be used to increase polymer chain length. In doing so, the thermal, and mechanical properties of polymers may be enhanced [40]. This is in addition to self-healing properties. According to Xie *et al.* [40], the first self-healing solid state block copolymer was achieved by Guan *et al.* [43] with hydrogen bonding agents at chain ends .According to the researchers, effective recovery of

extensibility and mechanical strength are achieved through microphase-separated supramolecular block copolymers which combine the toughness and stiffness of elastomer thermoplastics by incorporating the dynamic hydrogen bonds [40,43]. Yao *et al.* [44] report a hydrogen bonding agent ending siloxane oligomer which shows water enhanced healing properties [40,44]. The researchers credit the high concentration of multiple hydrogen bonding interactions for the material's mechanical properties and healing behavior [40,44].

As mentioned, another option for hydrogen bonding incorporation is within polymer side chains [40]. Li *et al.* [45] showed a polyurethane elastomer capable of self-healing with, "dynamic, super tough, and self-healing properties." [40] Increasing the hydrogen bonding additive mole percentages also increased mechanical properties such as strength, modulus, elongation, and toughness with a healing efficiency of 90% [40,45]. Additionally, as previously mentioned, self-healing may be achieved by incorporating hydrogen bonds within branching chains of polymers. Wu *et al.* [46] achieved a self-healing material within random hyperbranched polymers with a high density of hydrogen bonds, effective at room temperature [40,46]. According to Xie *et al.* [40], "internal molecular fragments in glassy hyperbranched polymers are highly restricted and have low molecular mobility, while the external branching units and the end groups have high mobility." The authors Wu *et al.* [46] introduce various complementary hydrogen bonding groups that attain self-healing via external sidechains and terminal groups of the polymer, using amino, amide, and other functional groups in high density [40].

Applications of self-healing elastomers which employ hydrogen bonding mechanisms are becoming vast. The aforementioned Bao group employed their materials for applications regarding conductive films with high stretchability [40,41] that can be utilized as electrodes. Both Bao *et al.* [41] and Kang *et al.* [24] used their self-healing elastomers within E-skin biomedical applications

[24,41]. The self-healing material synthesized by Chen *et al.* [47] was employed as a triboelectric nanogenerator. Both Wang *et al.* [48] and Pena-Francesh *et al.* [49] realized the potential of their self-healing materials as actuators. Xu *et al.* [50] utilized their self-healing material as bio-interfacial election.

2.4 Summary

With the objective of characterizing size, impact velocity, and penetration depth of MMOD, sensors must be developed which will be placed within the multi-layered SGA. Due to the nature of SGA inflatable structures, ideal sensors must be flexible, stretchable, and operate under low-power conditions. With these goals in mind, soft dielectric elastomer (DE) strain sensors are being explored due to their favorable properties. As maintenance and repairs on inflatable space structures may be costly, dangerous, and expensive, the ability to self-repair can be extremely beneficial. As a commonly utilized material for both dielectric substrates of soft DE sensors and self-healing materials, PDMS elastomer will be evaluated. Avoiding self-healing mechanisms which require a more difficult synthesis, and as a well explored self-healing mechanism within literature, with a low-difficulty synthesis, low cost and readily available materials, hydrogen bonding as the mechanism of self-healing will be employed.

3 Methodology

Within this chapter, the methodology of this research will be described. This chapter will cover the phases of research, materials used, material synthesis, iterations of sensor fabrication, and characterization methods. Research Approach.

3.1 Research Approach

In this work, a novel stretchable self-healing composite DE sensor was developed and characterized by analyzing capacitance change due to an applied load, a reduction in electrode surface area, and hypervelocity impact testing. Additionally, the sensor's ability to produce a measurable voltage during impact will be investigated. Furthermore, the DE sensors self-healing efficiency will be evaluated over time following sensor penetration.

The initial research phase will focus on additive manufacturing through synthesizing self-healable dielectric elastomers. The newly made elastomer will be characterized to ensure that it will meet the requirements of the project objective. The second research phase will focus on constructing parallel-place capacitance sensors, first with regular PDMS, as a proof of concept, followed by the synthesized self-healing material. The process for manufacturing this sensor will be evaluated and optimized to decrease manufacturing time and increase the ease of the manufacturing process. Phase three will focus on the evaluation of the manufactured sensor. This will include evaluating the self-healing qualities of the elastomer, testing the sensitivity of the sensor, and subjecting the sensor to hypervelocity impact testing and evaluation.

3.2 Self-Healing Material Synthesis

This research employed intrinsic self-healing methods which require no external stimuli. This was completed by including multi-strength (strong and weak) hydrogen bonds within the supramolecular network of the elastomer. PDMS was the base elastomer be used as the

crosslinking network to contain the healing agents will be PDMS. The PDMS employed contained amino end-groups to facilitate its reaction with the chosen additives, specifically aminopropyl terminated polydimethylsiloxane. The agent that employs strong hydrogen bonds, elasticity, and robustness is 4,4'-methylenediphenyl isocyanate (MPU), a solid. The agent which employs weak hydrogen bonds and the ability to dissipate strain energy through spontaneous, reversible, bond breaking and reformation is isophorone diisocyanate (IU), a liquid. This has been referred to as MPU-IU-PDMS by Kang *et al*. [24]

The amount of MPU-IU-PDMS made, and the amounts of MPU and IU additives used, may be determined through molar ratio calculations. The synthesis was completed within a fume hood. The necessary chemicals for this reaction are aminopropyl terminated polydimethylsiloxane of molecular weight ~5000 g/mol, 4,4'-methylenediphenyl isocyanate (MPU), isophorone diisocyanate (IU), chloroform solvent, and methanol. The one-pot synthesis procedure of this material is as follows.

Using a balance, 0.5g of MPU is obtained. In an Erlenmeyer flask, 15mL of chloroform solvent and a magnetic stir bar are added. The MPU was added to the Erlenmeyer flask, the flask was capped, and allowed to stir for 24 hours using a magnetic stirring plate, which allowed the MPU to fully dissolve. The following day, 100mL of chloroform solvent was measured and added to a 300mL round bottom flask, after the flask is secured. 33mL of aminopropyl terminated PDMS was measured and added to round bottom flask with the solvent. Using a mechanical stirrer, the PDMS is allowed to fully dissolve. Next, using a 1mL syringe, 0.76mL of IU was obtained. After this, using a pipette, the dissolved MPU was transferred to the round bottom flask in dropwise fashion. Next, the 0.76mL of IU was added to the flask, maintaining stirring the entire time. The contents of the flask were allowed to stir for five days inside the fume hood. After five days of stirring,

15mL of methanol was measured. The methanol was added to the round bottom flask and its contents were allowed to continue stirring for 30 minutes to quench the reaction. After the 30-minute period, the mechanical stirrer was stopped and removed from the round bottom flask. To remove excess unreacted isocyanate groups, another 15mL of methanol was measured and poured into the round bottom flask. A clear/white precipitate formed after 15 to 20 minutes. A pipette was used to remove and dispose of the precipitate in a designated hazardous waste container. Next, 30mL of chloroform solvent was measured and added the round bottom flask to redissolve the elastomer through a short five-minute stir. The process of excess isocyanate precipitation, removal, and re-dissolving of the elastomer was repeated three to five times until no excess isocyanates could be seen.

Now that the self-healing material has been synthesized but remains dissolved in the solvent, the solvent may be removed in two ways. The first method of removing the solvent is via a rotary evaporation using a Bucher Rotavapor. The disadvantage of this method is the time necessary to completely remove the solvent, more than 24 hours. Additionally, if all of the solvents are removed in this manor, the elastomer will be left inside of the round bottom flask. This makes the removal and further processing of the elastomer very difficult. The second option for removing the solvent is through simple evaporation. This method is much faster than using the rotary evaporation technique, usually taking around five to six hours. The necessary steps taken to employ this method were as follows.

After removing all excess unreacted isocyanate groups, the dissolved elastomer was poured into a 200mL beaker. An oil bath was constructed over a hot plate, placing a thermometer inside the oil bath. The hot plate was heated to 110°C. This heated the oil bath to approximately 50-55°C, which was monitored with a thermometer. Using clamps and the stand attached to the hot plate,

the beaker with the dissolved elastomer was lowered into the oil bath, but not allowed to touch the bottom of the container holding the oil, as this would apply too much heat. This action allowed for even heating of the elastomer within the beaker. Next, the mechanical stirrer was lowered into the beaker and allowed to stir slowly, preventing the solvent from boiling too quickly and overflowing into the oil bath. The material was monitor constantly to ensure this did not happen. After five to six hours, the volume of material within the beaker was once again matching the original amount of aminopropyl terminated PDMS used. After this occurred, the heat was turned off, the mechanical stirrer was removed, and the beaker with the elastomer was from the oil bath. At this temperature, the elastomer remained free flowing with a miniscule amount of solvent remaining. The contents of the beaker were poured into a mold of desired dimensions. Finally, the mold containing the elastomer was placed into a vacuum oven. The temperature was set to 50°C and vacuum was pulled until the oven read ~300mmHg. The elastomer was left in the vacuum oven overnight. The following day, the vacuum was released, the heat was turned off, and the mold was removed from the oven. The material was allowed to cool for one hour before proceeding with the desired method of characterization.

3.3 Parallel-Plate Capacitor Fabrication

This section chronologically details the iterative process of sensor fabrication throughout the project. First, fabrication using Sylgard 184 is described, followed by fabrication using the self-healing elastomer, and the improvements made regarding that process. A fiberglass fabric was included, creating a composite sensor, within the elastomer for multiple reasons. First, as mentioned previously in section 2.2.1, the addition of materials of high permittivity between electrodes of a parallel-place capacitor will result in an increase in capacitance, as can be seen from the governing equation 2. Fiberglass fabric is a material with high permittivity and will aide in the sensitivity of the fabricated sensor. Furthermore, the fiberglass fabric which extends beyond

the boundaries of the electrodes will facilitate the sensors integration into test fixtures, and possibly a soft goods assembly in the future. Figures showing the results of each iteration will be included in the following chapter. Each iteration will be described as iteration one, iteration two, etc. Figure 3.1 on the following page shows the proposed sensor setup.

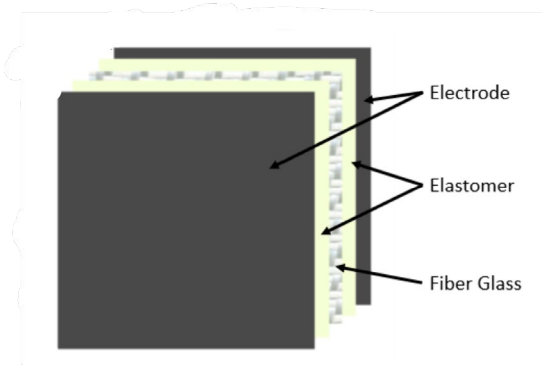

Figure 3.1 Dielectric elastomer sensor as proposed by this research.

In iteration one, Sylgard 184 is chosen for initial proof of concept for multiple reasons. It is readily available and mechanically analogous to the self-healing elastomer being synthesized. Initially, a mold of desired dimensions is cut from polycarbonate. This material is chosen as it is readily available and will not chemically bond with the Sylgard 184. The mold is cut from polycarbonate in such a fashion that it will create two halves of a single mold, in which the elastomer and fiberglass fabric are be contained. Sylgard 184 is poured into both halves of the mold. The fiberglass fabric is placed over one of the mold halves, and the other half of the mold is placed on top of the fabric and the first mold. The assembly created is then clamped together and placed into a vacuum oven. The oven is heated to 50°C and vacuum is pulled to ~300mmHg. This is left for 24 hours under heat and vacuum in a vertical orientation. The assembly is removed from

the vacuum oven, allowed one hour to cool, and finally removed from the mold successfully. A diagram of this molding process is shown in Figure 3.2.

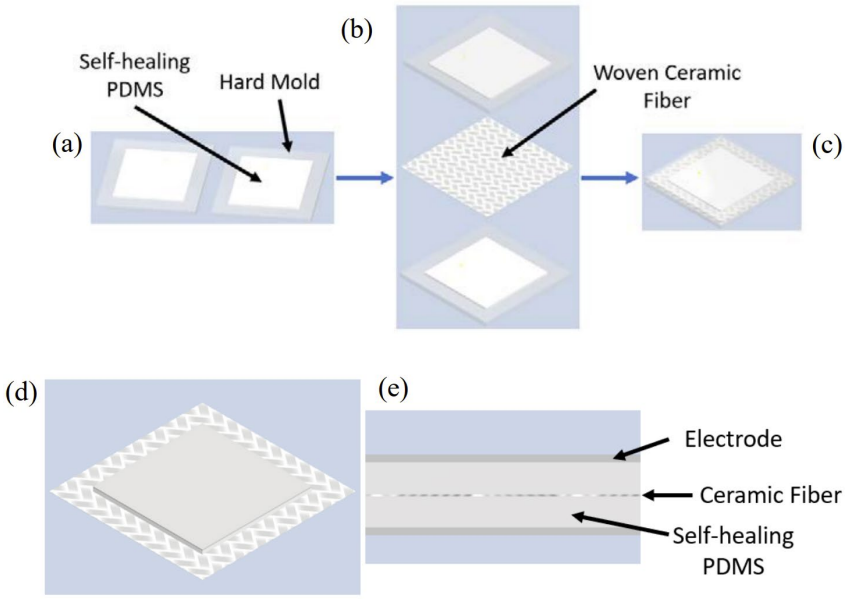

Figure 3.2 Sensor molding process.

In iteration two, using synthesized MPU-IU-PDMS in a molten state, the same procedure is completed. Due to complications which are detailed in the following chapter, a new procedure for fabricating the fiberglass fabric elastomer sandwich is established. In iteration three, a single silicone mold is employed. Immediately after removing solvent from the elastomer, half of the necessary MPU-IU-PDMS is poured into the mold and allowed to harden in a vacuum oven as described above in section 3.2. Next, the fiberglass fabric is pressed into the elastomer in the mold. The remaining MPU-IU-PDMS is poured into the mold over the fiberglass fabric. The mold and its contents are again placed into the vacuum oven under the same conditions and for the same duration of time. The next day, the mold is removed from the oven and allowed one hour to cool. Finally, the material is removed from the mold for further processing.

Following the fabrication process described above, electrodes are placed on the outside of the elastomer layers to form the parallel-plate capacitance sensor. Initially, in iteration one, solid stainless-steel electrodes are simply placed to determine a capacitance and ensure proper working order. Next, in iteration three, given the requirements for implementation in an SGA, soft, flexible, and stretchable electrodes must be employed. Due to being readily available, low cost, and given its mechanical qualities, woven conductive fabric electrodes are chosen and applied to the outer elastomer layers. The conductive fabric electrodes utilized are made of nickel and copper plated polyester.

3.4 Characterization Methods

First, to ensure the correct synthesis of MPU-IU-PDMS, Fourier-transform infrared spectroscopy (FTIR) is performed. This is done to ensure the consumption of isocyanate groups, indicating complete synthesis. To evaluate the self-healing ability of the synthesized elastomer, several tests are employed. The self-healing efficiencies of the elastomer will be determined through uniaxial tensile testing at room temperature to ensure healing is taking place. Once successful, the elastomer is cut and allowed to heal at -80°C to ensure healing will occur at low temperatures where its desired application will take place. The pristine and healed elastomers are then subjected to tensile stress measurements to determine self-healing efficiency at low temperatures. Additionally, a time-lapse study is completed to view the elastomer healing a digital microscope monitor.

Several methods are employed to characterize the parallel-plate capacitance sensor. First, pressure testing of the sensor will be employed to observe the initial resting capacitance using a Gw INSTEK LCR-6020 capacitance meter. Next, weights of varying masses from 0.45lbs to 3.45lbs are placed on the sensor, and the change in capacitance is recorded before converting the mass to force in newtons. This step helps to determine the change in capacitance due to a given

force, describing the sensitivity of the sensor upon impact. Next, holes are made through the sensor at a 1mm diameter to simulate impact and penetration by MMOD. The initial capacitance is recorded. As more material is removed, all layers included, the capacitance change is recorded, along with the area of electrodes removed. This further describes the sensitivity of the parallel-plate capacitance sensor. Due to the nature of this test and because material is physically removed, the samples utilized in this test are then monitored further to view how the MPU-IU-PDMS will fill the volume removed from the sensor. A diagram of both tests is shown below in Figure 3.3.

This setup is then further characterized through hypervelocity impact testing at the University of Dayton Research Institute (UDRI). A 5 mm diameter aluminum projectile is fired at 7 km/s into an array of three sensors. The voltage of all three sensors is monitored during impact using an oscilloscope. The results are used in attempt to back-calculate the velocity of the projectile. This will aide in determining the effectiveness of the sensor in a real-world application environment.

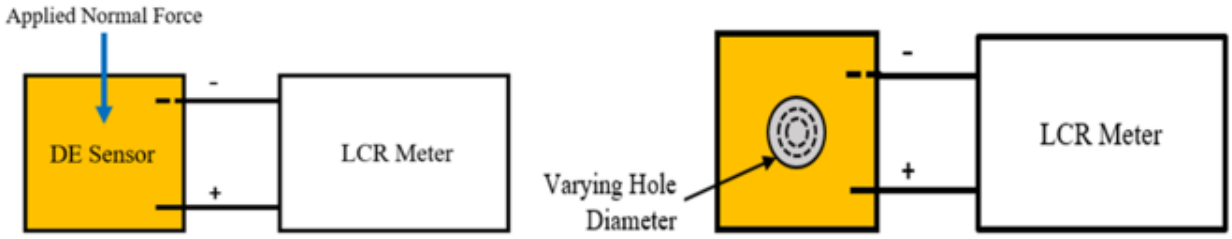

Figure 3.3 Applied force test (left) and electrode area removed test (right).

4 Results

Within this chapter, all results of characterization methods are outlined. Self-healing characterization results are followed by capacitance sensor results.

4.1 Self-Healing Characterization

Within this section, self-healing characterization results are shown in several ways. FTIR spectra are taken to confirm the consumption of isocyanate groups after material synthesis. The self-healing efficiency of MPU-IU-PDMS is determined via uniaxial tensile testing, as consistent with the literature. Time-lapse studies are completed to aide in visualizing the material healing process.

4.1.1 FTIR Characterization

Here, FTIR characterization is completed to show consumption of isocyante groups after synthesis. The result is shown on the following page in Figure 4.1.

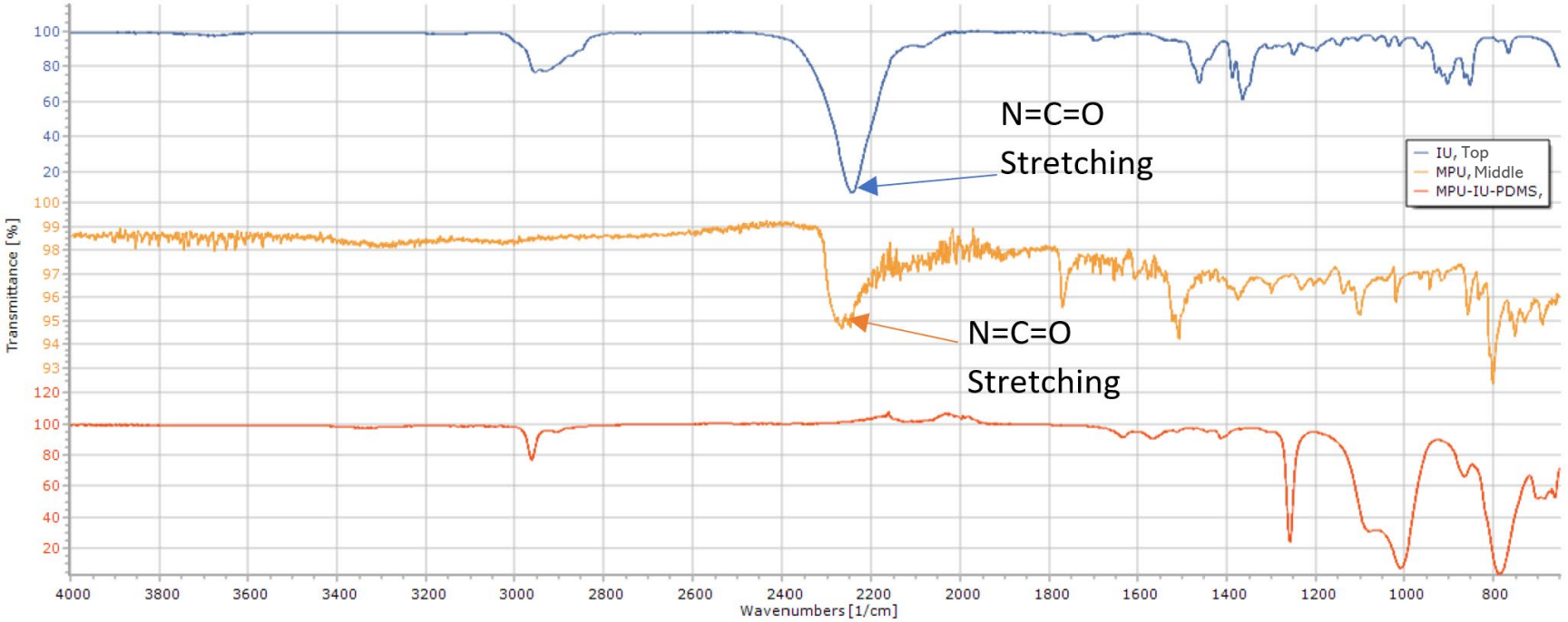

Figure 4.1 FTIR spectra showing MPU-IU-PDMS (red), 4,4'-methylenediphenyl isocyanate (MPU, orange), and isophorone diisocyanate (IU, blue).

4.1.2 Self-Healing Efficiency

To determine the self-healing efficiency of the synthesized elastomer, multiple uniaxial tensile tests are performed. One elastomer sample was cut in half and allowed to heal while the other was immediately tested. After 24 hours of healing time, the cut and healed sample is tensile tested under the same conditions as the pristine sample. The results of the room temperature self-healing efficiency tensile test are shown below in Figure 4.2 and discussed in the following chapter.

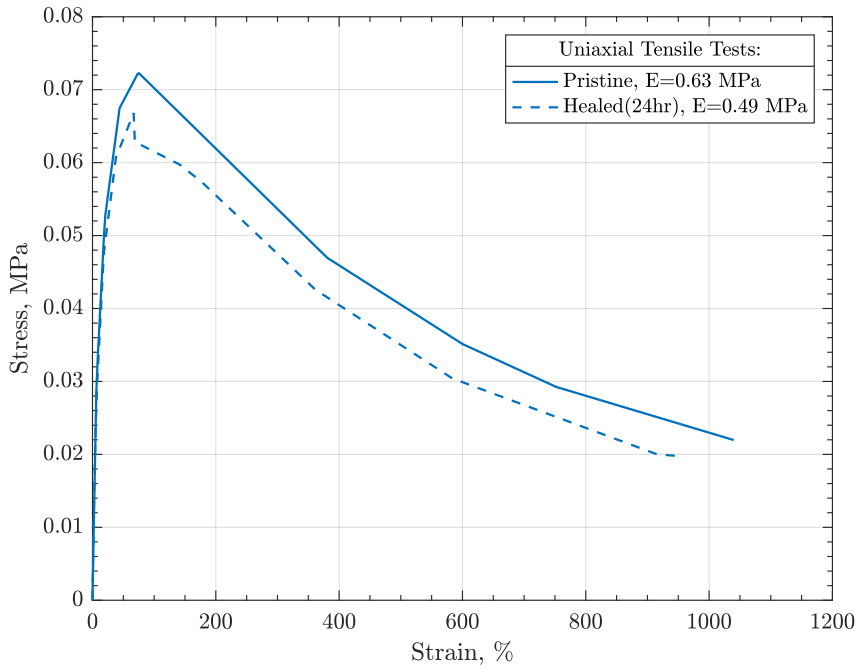

Figure 4.2 Uniaxial tensile tests: pristine sample (solid line) and sample healed for 24 hours (dashed line) at room temperature.

Figure 4.3 and Figure 4.4 are shown on the following page, and represent the two low temperature self-healing efficiency tests of MPU-IU-PDMS after healing for 24 hours at -80°C. The results on the following page are discussed in further detail in the next chapter.

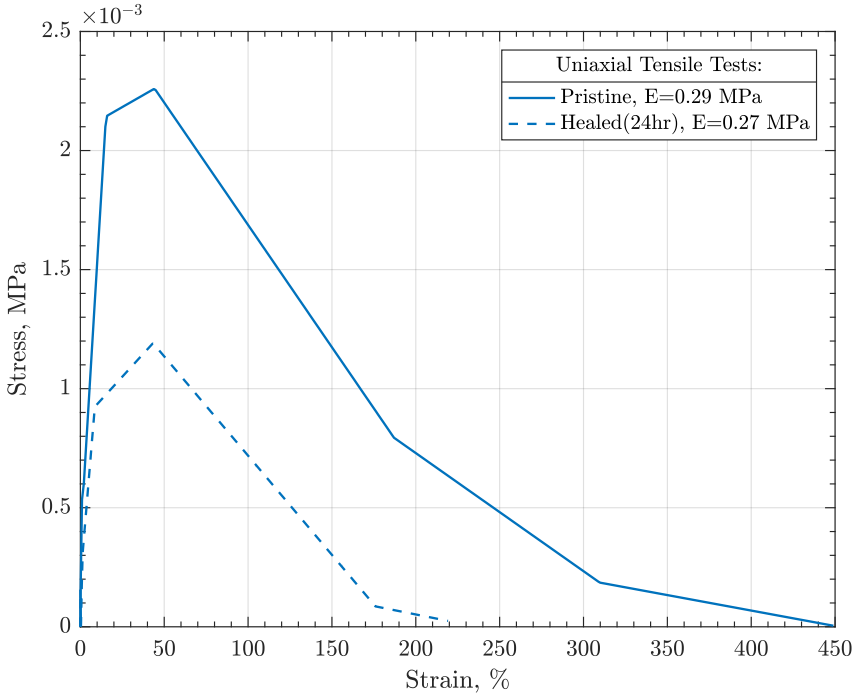

Figure 4.3 Uniaxial tensile tests, pristine sample (solid line), sample healed for 24 hours at -80°C (dashed line).

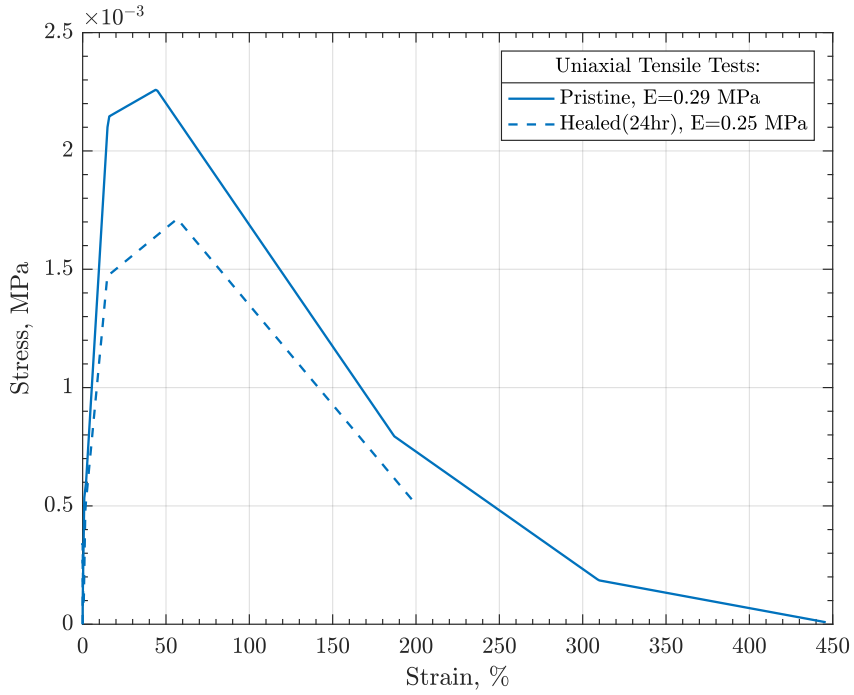

Figure 4.4 Uniaxial tensile tests, pristine sample (solid line), sample healed for 24 hours at -80°C (dashed line).

4.1.3 Time-Lapse Study

Self-healing results are demonstrated here via a time-lapse study. In this study, 10 cubic millimeters of material was removed from a 10 mm thick MPU-IU-PDMS sample, using a circular cutting tube with an area of one square mm. The sample was then allowed to heal while being monitored by a digital microscope. The results are shown on the following page in Figure 4.5. Image (a) shows the material immediately the after puncture. Image (b) shows the material 30 minutes after the puncture. Image (c) shows the material one hour after the puncture. Image (d) shows the material two hours after the puncture. Image (d) shows the material three hours after the puncture, when the hole is no longer visible to the naked eye. Image (f) shows the material four hours after the puncture, completely healed.

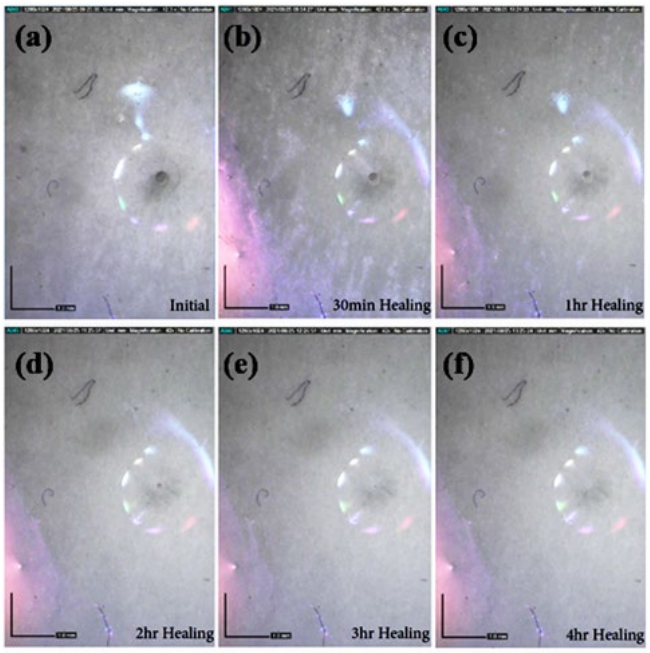

Figure 4.5 PDMS self-healing time-lapse study. (a-e) MPU-IU-PDMS at different healing intervals, initial, 30 min, 1hr, 2hr, 3hr, 4hr.

4.2 Parallel-Plate Capacitance Sensor

In the following sections, testing results of the parallel-plate capacitance sensor are shown. The results of the fabrication process are shown, followed by sensitivity measurements regarding force, penetration, and hypervelocity impact testing.

4.2.1 Parallel-Plate Capacitance Sensor Fabrication

The result of iteration one, using Sylgard 184, is shown in Figure 4.6. The top left image shows the initial deposition of Sylgard 184 into the mold. The top left image (a) shows material in the mold before vacuum oven heating. The top right image (b) shows the material after the heating and vacuum process. The bottom left and right images (c,d) show the material after being removed from the mold. While results of iteration were promising, the removal of self-healing material from the mold in iteration two proved unreliable. The material often could not be removed from the mold without irreparably deforming or ripping the sensor apart.

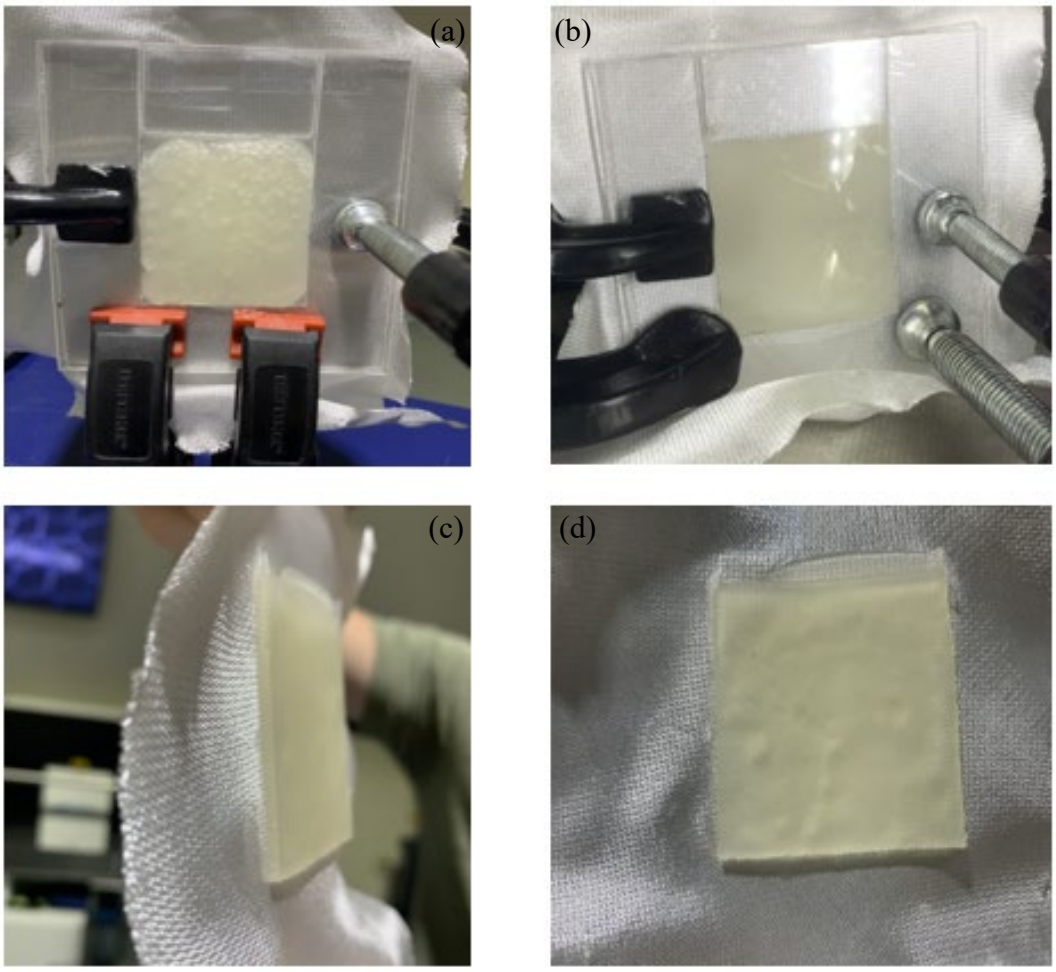

Figure 4.6 Images of sensor fabrication during iteration one. (a) Material initially poured into mold. (b) Material after vacuum oven heating. (c,d) Material after removal from mold.

In iteration three, a new process was implemented. Using a single silicone mold proved to be a far more consistent process. The results of this method are shown in Figure 4.7.

The top left image (a) shows the first half of the sensor with fiberglass fabric pressed into the material. The remaining three images, top right (b), and bottom (c,d), show the result of the vacuum oven process with hardened material.

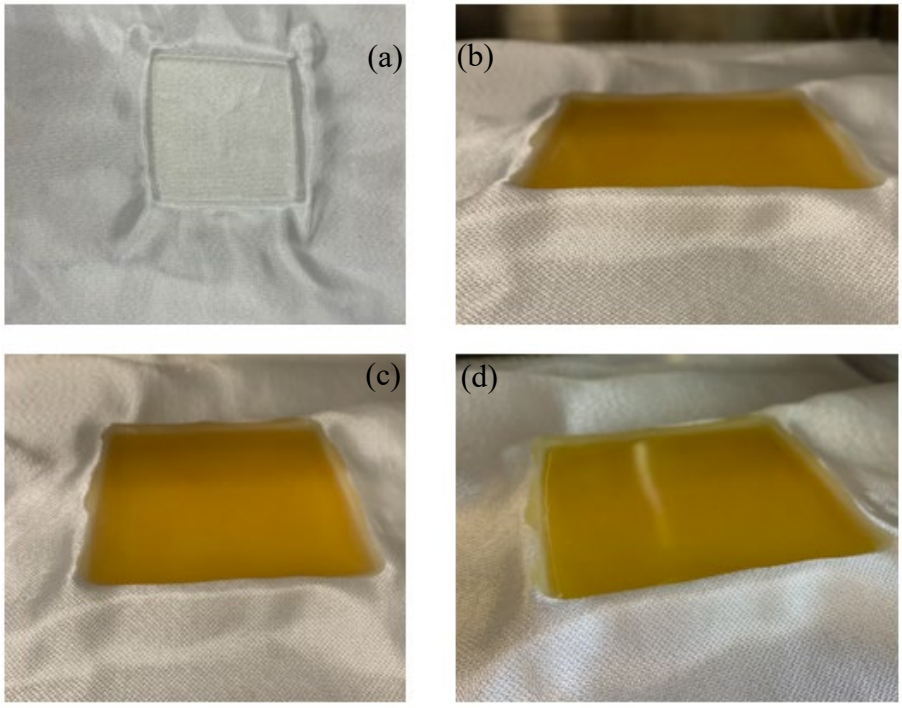

Figure 4.7 Iteration three sensor fabrication process. (a) Fiberglass fabric on top of half of elastomer. (b-d) Material after vacuum oven heating.

Following the fabrication of the fiberglass and self-healing elastomer sandwich, flexible fabric electrodes are applied. Next, wiring connections are attached with copper tape, followed by Kapton tape to fully encapsulate the sensor and complete fabrication. This result is shown in Figure 4.8.

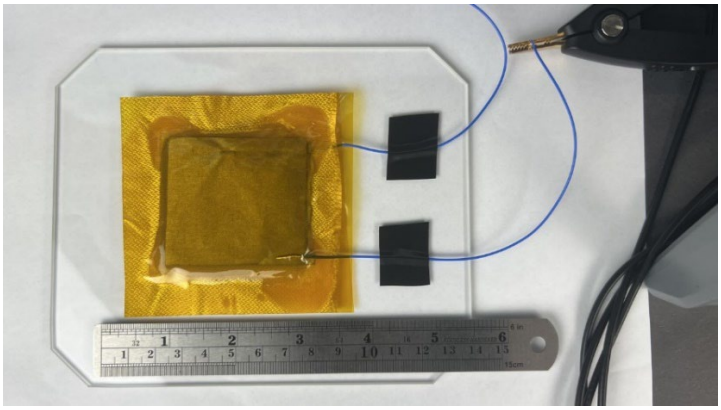

Figure 4.8 Final result of iteration three sensor fabrication.

4.2.2 Applied Force and Capacitance Change

To test the sensitivity of the fabricated sensor, masses are applied to the sensor in a uniform area as capacitance is monitored using a Gw INSTEK LCR-6020 capacitance meter. The meter settings used are an average of 16 measurements, slow speed, at 1kHz. The test is performed 4 times; average and standard deviation results are plotted below in Figure 4.9.

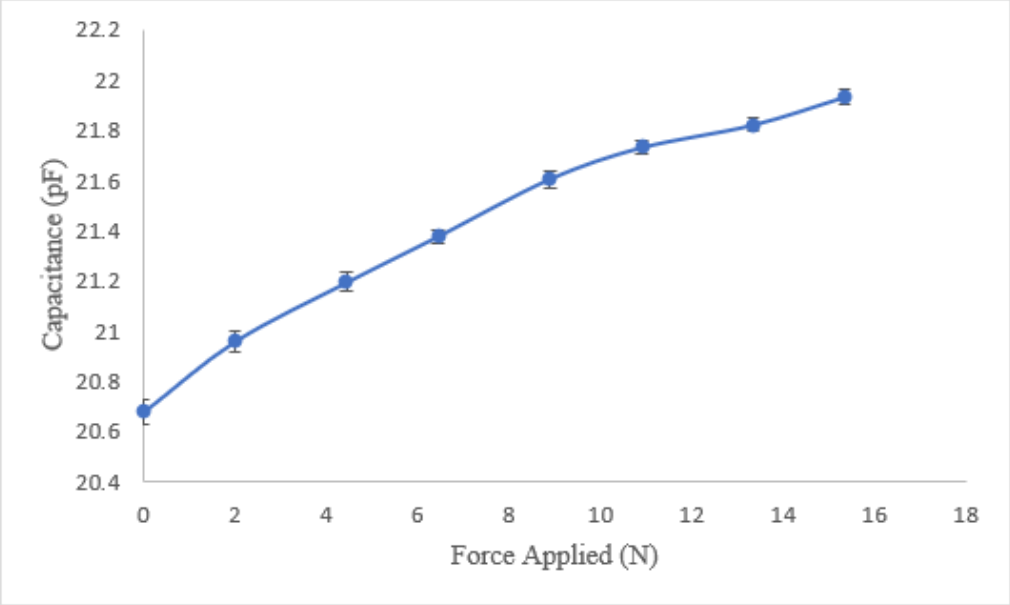

Figure 4.9 Change in capacitance due to the applied force.

4.2.3 Area Removed and Capacitance Change

Additional testing is done to determine the sensitivity of the fabricated sensor when penetrated. This is done by removing the area from the sensor to simulate an impact which causes complete the removal of the sensor material. This test is also completed using the Gw INSTEK LCR-6020 capacitance meter. Once again, the meter settings used are an average of 16 measurements, slow speed, at 1kHz. The results are shown in Figure 4.10. Additionally shown in Figure 4.11, are images taken one week after the test, showing the holes in the sensor post-healing.

All holes in the sensor as a result of the test are completely filled with the self-healing MPU-IU-PDMS.

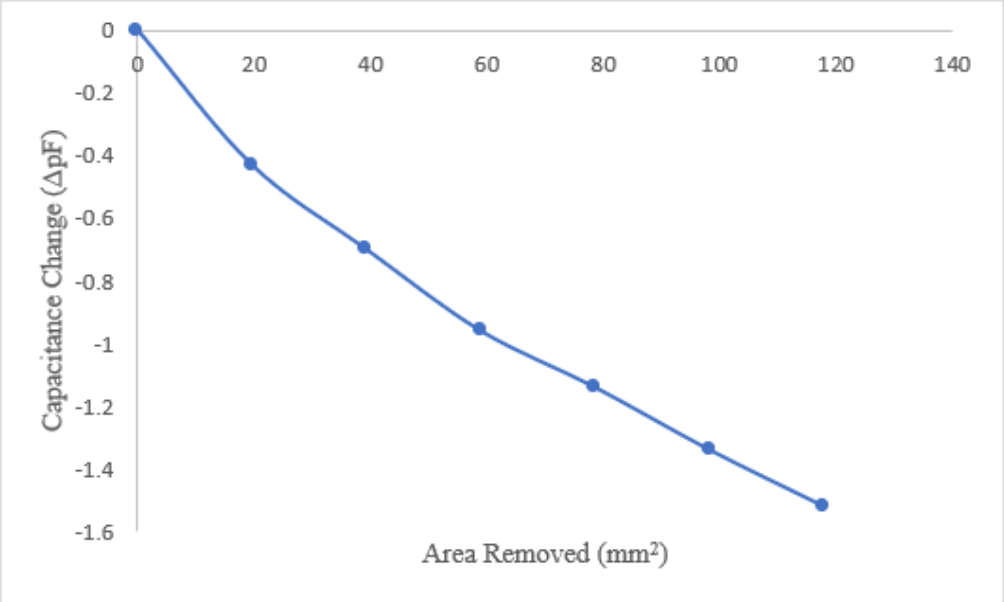

Figure 4.10 Capacitance change due to the area of sensor removed.

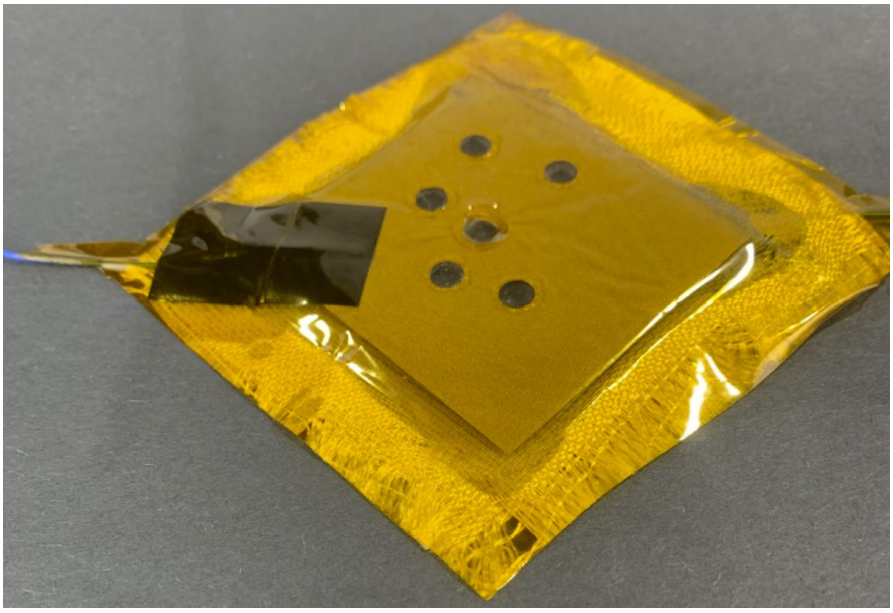

Figure 4.11 Healed sensor one week after capacitance change due to the area removed.

4.3 Hypervelocity Impact Testing

Hypervelocity testing was completed at the University of Dayton Research Institute (UDRI). First, the sensors were incorporated into a frame which was compatible with the UDRI testing chamber. The sensors were sandwiched between aluminum frames and secured using two-part Aeropoxy PR2032 and PH3665 epoxy resin and hardener. This is shown in Figure 4.12.

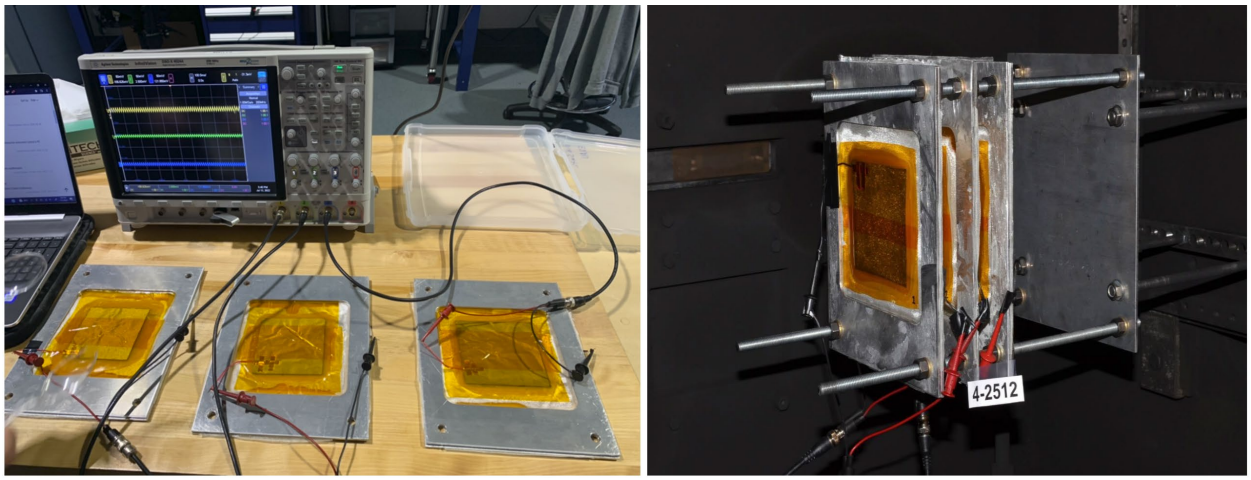

Figure 4.12 (a) Setting up trigger system. (b) Sensors incorporated into frame for hypervelocity impact testing.

In the hypervelocity testing done at UDRI, a 5 mm diameter projectile was fired at the array of sensors at 7 km/s, or 15,659 mph. The capacitance was measured before and after the test. Additionally, the voltage of the sensors was monitored during the test. The voltage was monitored using an Agilent InfiniiVision DSO-X-4024A Digital Storage Oscilloscope. Settings used during this test are 50mV, 2.5 giga samples per second, at 200 MHz, giving the best visualization of the data during the test. The voltage data obtained from the test is shown in Figure 4.13. The forward sensor is shown in blue, the middle sensor is shown in red, and the aft sensor is shown in yellow. The initial impact is indicated within the figure using an asterisk. Further exploration of the voltage

data obtained revealed a projectile velocity of 5.67 km/s between the forward and middle sensor, and a projectile velocity of 1.80 km/s between the middle and aft sensor.

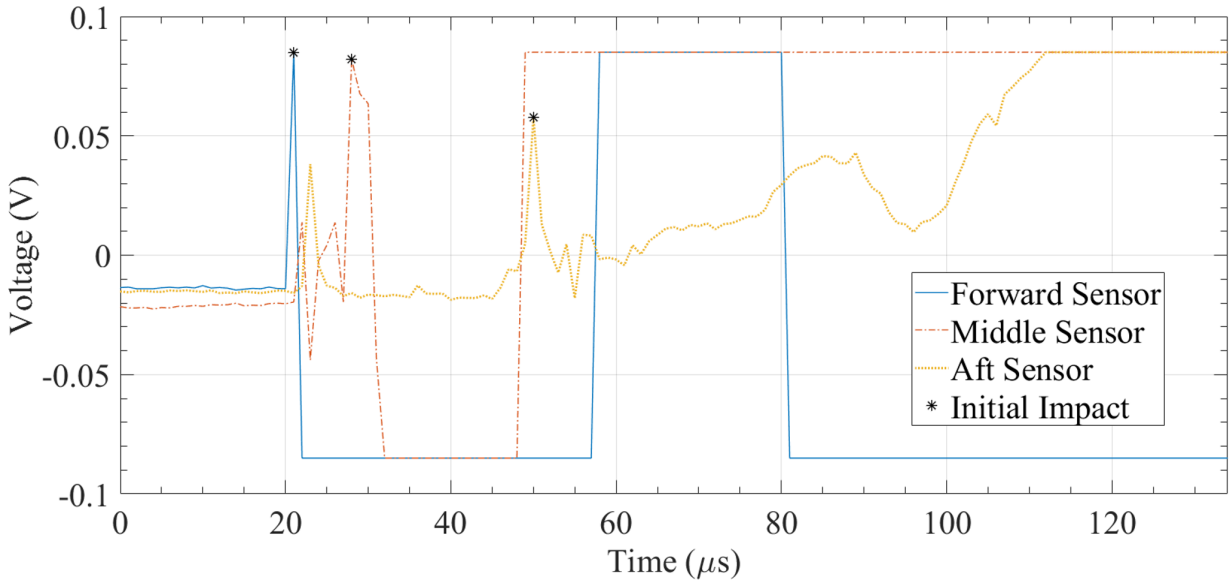

Figure 4.13 Voltage data obtained during hypervelocity impact testing.

Capacitance measure before the test was 67.0 pF, 67.2 pF, and 47.5 pF, respectively, for the forward, middle, and aft sensors. Following the test, no capacitance could be detected. This is due to a byproduct of the test and will be discussed further in the following chapter. The damage inflicted to all the sensors is shown in Figure 4.14 and Figure 4.15. Figure 4.14 shows the sensor damage immediately after the test from (a) frontal view and (b) side view. Figure 4.15 shows the forward (a), middle (b), and aft (c) sensors respectively from left to right after being removed from the test frame. Two pages following, Figure 4.16 shows the X-ray imaging done during the hypervelocity test at UDRI.

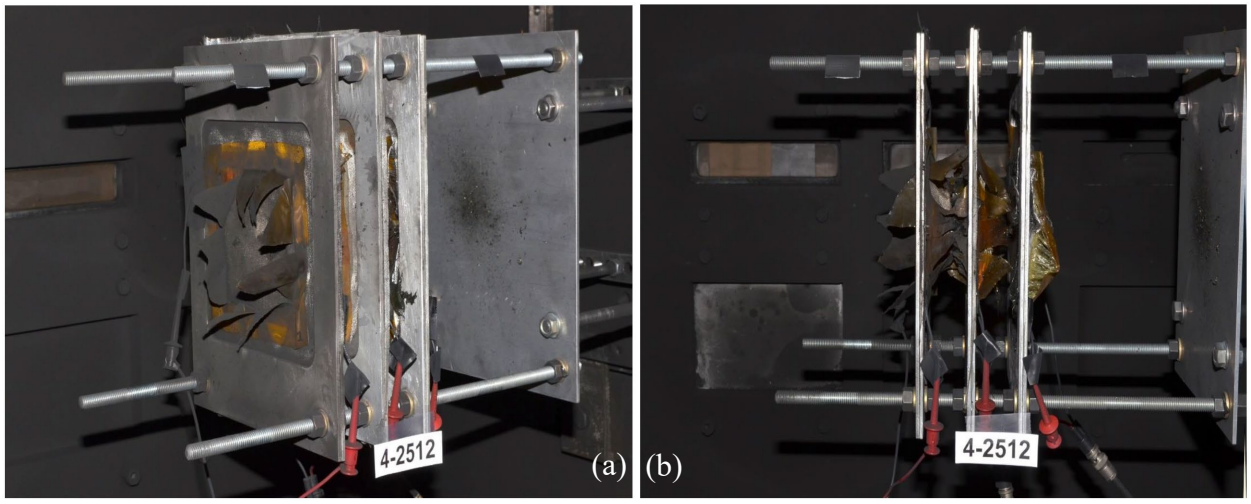

Figure 4.14 Sensor damage immediately after hypervelocity test. (a) Frontal View. (b) Side view.

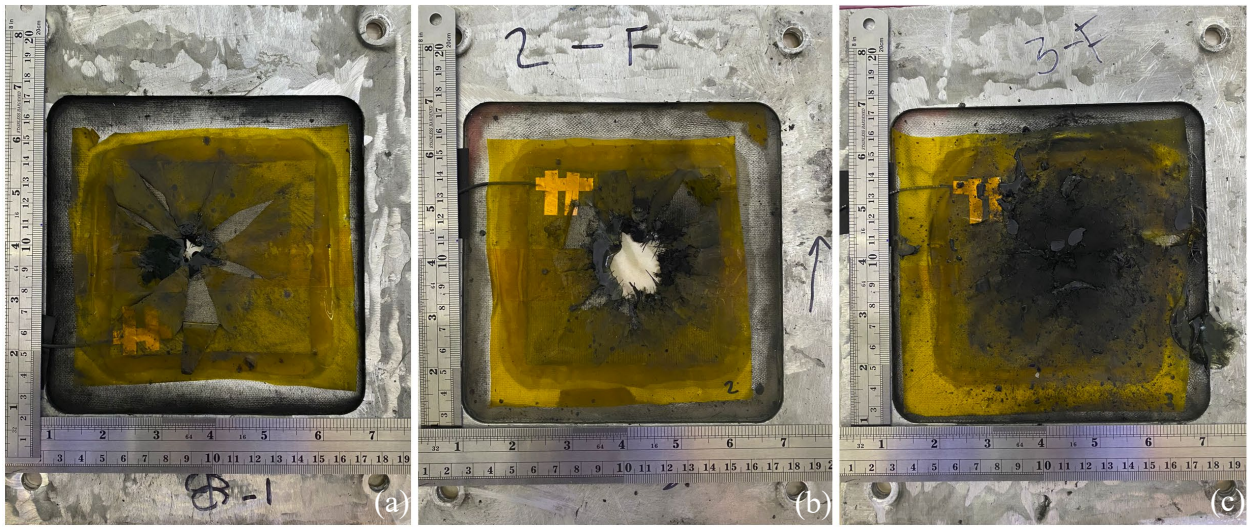

Figure 4.15 Sensor damage after removal from test frame. (a) Forward sensor. (b) Middle sensor. (c) Aft sensor.

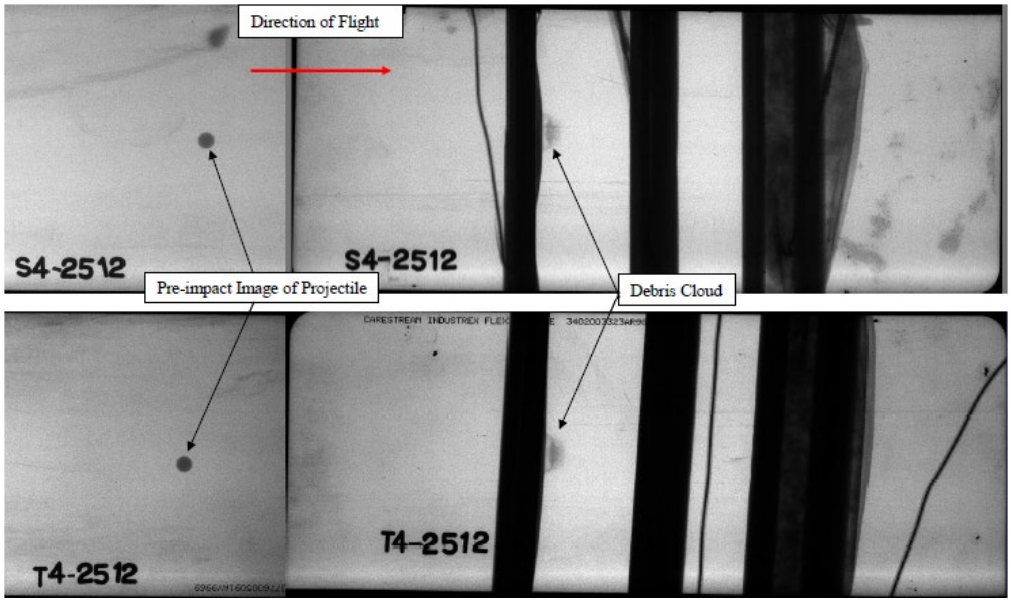

Figure 4.16 X-ray imaging during hypervelocity test at UDRI.

After returning from UDRI, the sensors are allowed to heal. The sensors are imaged one and three weeks after testing to visualize healing. The hole created in the middle sensor is not expected to heal due to extreme size. As can be seen in the above Figure 4.14, the aft sensor has expanded from the inside. This expansion from the inside be the prime healing interest of aft sensor. The focus on the forward sensor will be to heal the entirety of the area removed due to projectile penetration. These results are shown in Figure 4.17 and Figure 4.18 on the following page. Figure 4.17 shows the forward sensor, and front and back of aft sensor respectively from left to right.

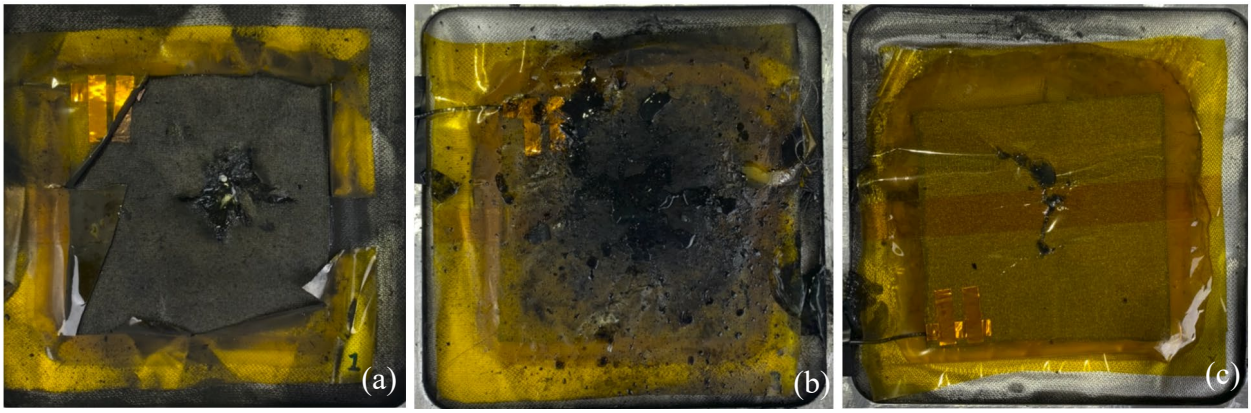

Figure 4.17 Sensor healing one week after hypervelocity test. (a) Forward Sensor. (b) Front of aft sensor. (c) Back of aft sensor.

Figure 4.18 below, taken three weeks after hypervelocity testing at UDRI, shows the front and back of the front sensor and the after sensor from left to right respectively.

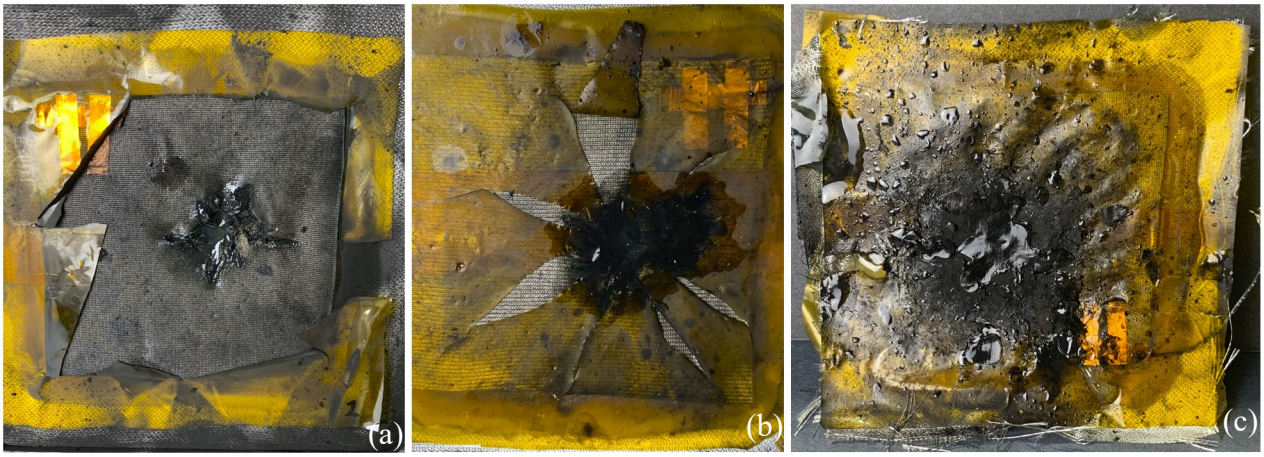

Figure 4.18 Sensor healing three weeks after hypervelocity test. (a) Front of forward sensor. (b) Back of forward sensor. (c) Aft sensor.

All results shown above will be discussed in the following Chapter 5: Discussions, Conclusions, and Recommendations.

5 Discussions, Conclusions, and Recommendations

Herein, the results shown in the previous chapter will be discussed in further detail. In addition, conclusions will be drawn regarding the project as whole. Lastly, recommendations will be made for future research which may be carried out.

5.1 Discussion

In the previous chapter, Figure 4.1 depicts the FTIR spectra taken of MPU-IU-PDMS, and its additive molecules used during synthesis. The disappearance of the MPU and IU peaks containing the N=C=O end-groups around 2300 1/cm [51] confirm that the material synthesis has been completed, and all isocyanate groups have been consumed and reside within the new polymer chain.

Next, as shown in Figures 4.2, the self-healing efficiencies of MPU-IU-PDMS has been determined. Given the results of the test with samples healed at room temperature, the self-healing efficiencies can be calculated based upon equations 3-5. Taking Young's Modulus into consideration, it was found that η_E = 77.78%. Considering maximum tensile strength, the calculated self-healing efficiency $\eta_{\sigma_{max}}$ = 91.27%. Finally, the self-healing efficiency regarding maximum strain was calculated as $\eta_{\gamma_{max}} = 91.31\%$.

Additionally, given the environment of the desired end-application of the sensors, self-healing tests have been conducted by allowing samples to heal at -80ºC for 24 hours. This is the coldest environment available on the Embry-Riddle Daytona Beach campus. This is shown in the previous chapter in Figure 4.3 and Figure 4.4. As with the test completed at room temperature, their self-healing efficiencies are calculated using equations 3-5. Multiple tests were performed as healing at low temperatures is imperative in the application. For tests one and two, η_E = 93.10% and 86.21%. Considering maximum tensile strength, the calculated self-healing efficiency $\eta_{\sigma_{max}}$ =

52.04% and 75.64%. Finally, the self-healing efficiency regarding maximum strain was calculated as $\eta_{\gamma_{max}} = 43.93\%$ and 37.87% The increase in Young's Modulus from the room temperature to low temperature self-healing efficiencies is attributed to a decrease in polymer chain mobility. This is due to the extreme reduction in temperature. The reduction in the healing efficiency of maximum strain in MPU-IU-PDMS is also due to the same reason. Healing and storage at -80ºC for 24 hours causes a reduction in chain mobility that will not allow chains to untangle and stretch to the same degree.

Next, to visualize the MPU-IU-PDMS healing over time, a time lapse study is completed as shown in Figure 4.5. After only three hours, the hole is no longer visible to the naked eyed. After four hours, the hole is completely healed at room temperature. With 10 cubic millimeters of material being removed, the displayed healing is at a rate of nearly two cubic millimeters per hour.

Figure 4.6 and Figure 4.7 show the evolution of the sensor fabrication throughout the project. After the final fabrication method was determined and enacted, as seen in Figure 4.7, the final dimensions of the sensor are as follows: 10 cm by 10 cm by 0.5 cm regarding length by width by height. In addition to this, the progressive search the for the best electrode material was vital. Initially, simple metal electrodes were used to confirm the ability to create a capacitance that would change upon applying pressure. After this was confirmed, conductive carbon paint was considered. This material quickly dried and would crack when the sensor flexed. In consideration of the sensor's application on inflatable structures, this material was no longer considered. It was finally decided that a flexible conductive fabric would best suit the sensors application environment. Copper and nickel-plated polyester was chosen for their low cost, flexibility, and ease of application to the MPU-IU-PDMS.

Following the optimization of the sensor fabrication, the sensor's sensitivity was explored by applying force to the sensor. In this experiment force is applied to the sensor under a uniform area. The capacitance meter settings include an average of 16 measurements, at slow speed, and at 1kHz. This is shown in Figure 4.9. The test is completed four times. The average of the four tests is used as the capacitance value, at eight different force value, making a total of 32 measurements. The standard deviation is calculated as well and appears in the figure. The results are desirable, showing a nearly linear trend with small standard deviation, making the measurements very reliable in detecting impacts. This also follows the expected trend of the governing equation 2; when the distance between electrodes is decreased due to compression, the capacitance should, and does, increase.

Additionally, in Figure 4.10, the sensitivity is determined for detection of projectile penetration. As area is removed from the electrodes, the capacitance is recorded. The trend shown in Figure 4.10 is nearly linear as well and follows the expected trend of the governing equation 2. As the area of electrode is decreased, simulating a complete penetration of the sensor, the capacitance should, and does, decrease. These combined results allow determination of impact, by capacitance spike due to the force of impact, followed by capacitance decrease from the original value, relaying that the projectile has penetrating the sensor, and allowing for determination of damaged area through back-calculation. One week after the material was removed from the sensor in the test, shown in Figure 4.11, the MPU-IU-PDMS has completely filled in the missing area. This evidence further supports the self-healing results of the MPU-IU-PDMS implemented in the sensor platform.

Figure 4.12 shows the preparation of the sensors for hypervelocity impact testing at the University of Dayton Research Institute. First, using the fiberglass fabric within the sensor, the

sensors are secured to the metal frame using aerospace grade epoxy. The sensors are connected to an oscilloscope, showing a voltage measurement. This is also used to monitor impacts on the sensor. A laser trigger is used to begin recording the voltage data immediately before impact occurs. The frame secured within the impact chamber is also shown in Figure 4.12.

The voltage data obtained during the hypervelocity test is shown in Figure 4.13. As marked by an asterisk for each sensor, the exact time of impact is shown. The voltage spikes are large and can be easily seen. With the distance between the sensors known, using the voltage and time data, the average velocity of the projectile can be calculated. The velocity of the projectile between the forward and middle sensor is found to be 5.67 km/s. The velocity of the projectile between the middle and aft sensor is calculated as 1.80 km/s. This confirms the sensors' ability, using voltage, to determine the exact time of impact as well as the speed of the projectile. The projectile before impact of the forward sensor, and after impact, creating a debris cloud, can be seen in Figure 4.16. This is the X-ray imaging performed during the test.

Though capacitance data was collected before the test, no capacitance could be measured after, as the sensors shorted. According to Mr. Kevin Poormon, the manager of the hypervelocity gun, carbon is a biproduct created during the test in high quantities. Upon further inspection of the sensors immediately after the test, as can be seen in Figures 4.14 and 4.15, the sensors are covered in carbon, including the inner MPU-IU-PDMS material. The conductive carbon creates an electrical connection from one electrode to the other, rendering the capacitance zero. As shown in Figure 4.15, inspection after the test confirmed that the wired connections where still intact, and the electrodes were not simply pushed together by the projectile. This serves to confirm the conductive carbon test biproduct is causing the sensor short. Additionally, after inspection of the sensors, it was determined that the damage done to the middle sensor by the projectile and debris

cloud cause damage that is too large to heal. Though the damage to the forward sensor was extensive, healing is not ruled out. Upon viewing the aft sensor, as can be seen in Figure 4.14, the sensor has expanded from the inside, tearing it apart from the middle. This is most likely due to a fabrication error, probably an air bubble that could not be seen or removed. The after sensor also contained a very small hole, which was covered in carbon. The aft sensor was still monitored for healing progress.

One week after returning from UDRI, the healing progress of the forward and aft sensors are examined. This is shown in Figure 4.17. The left image shows the forward sensor, where the damage is almost completely filled by the MPU-IU-PDMS. These results are extremely promising. The middle and right images show the front and back of the aft sensor. At this point in time, the small hole that was made, as can be seen in the right image, is completely healed. Additionally, the expansion of the sensor from the inside has almost completely disappeared. At the time of inspection, some small gaps remained, however extensive progress was made.

Three weeks the testing at UDRI, the healing progress is again inspected, shown in Figure 4.18. the left and middle images show the front and back of the forward sensor, respectively. Both sides show that the damage done to the sensor has been filled completely with MPU-IU-PDMS. The right image shows the aft sensor. Here the remaining small gaps through the center of the sensor have collapsed, rendering the sensor whole again. Visual and physical inspection reveal that the sensor has regained its structural integrity. The results of the healing process are quite substantial when considering the initial damaged shown in Figures 4.14 and 4.15 The sensors remain unable to give a capacitance reading due to the extreme permeation of carbon throughout the elastomer.

5.2 Conclusion

As micrometeoroids and orbital debris which cannot be tracked by NASA pose a serious threat to orbital space structures such as inflatables, this research has proposed and created a structural health monitoring system in attempt to mitigate this threat. A self-healable elastomer, MPU-IU-PDMS, has been synthesized in house. The material achieves self-healing through multi-strength hydrogen bonding throughout the supramolecular network. This self-healable elastomer is used to create a parallel-plate capacitance sensor platform. Research results show the healing process in multiple ways and determined the self-healing efficiencies of the material at room temperature and -80ºC. Once more, the calculated self-healing efficiencies of the material are: η_E = 77.78%, $\eta_{\sigma_{max}}$ = 91.27%, and $\eta_{\gamma_{max}} = 91.31\%$ for Young's Modulus, maximum stress, and maximum strain respectively. More importantly, the MPU-IU-PDSM was successful at healing within 24 hours at low temperatures. The low temperature efficiencies are as follows: η_E = 93.10% and 86.21%, $\eta_{\sigma_{max}}$ = 52.04% and 75.64%, and finally $\eta_{\gamma_{max}} = 43.93\%$ and 37.87%. The sensitivity was determined and found favorable through tests which applied force to the sensors and removed area from the sensors. Results of the hypervelocity impact testing to simulate MMOD impact showed the ability to detect the exact time of impact and projectile velocity between sensors. In the weeks following the hypervelocity impact testing, further visualization of self-healing was shown in the two sensors which did experience critical damage. Through the implementation of a self-healable elastomer as a dielectric material in a parallel-plate capacitance sensor, it was shown possible, using capacitance and voltage measurements, that the platform can repair damage done by projectile impact, detect the force of impact, speed of impact, and relative damage done to the sensor. This will serve to keep astronauts who inhabit inflatable structures more informed as to the

state of their module, as well as reduce maintenance or replacement frequency. This in turns promotes safety and reduces operating costs.

5.3 Recommendations

This research recommends improving the scope of the project by exploring other methods of intrinsic self-healing, such as disulfide bonds or metal-ligand coordination. Further self-healing efficiency tests should be conducted over a range of times longer than 24 hours to evaluate and compare the improved healing progress of the material. Additionally, to improve the research, it would be beneficial to conduct more capacitance sensitivity studies in which area is removed while capacitance is monitored. Additionally, further sensitivity tests of both varieties, force applied, and area removed, should be completed to determine if the capacitance will saturate over time. This will aide in confirming the reliability of the sensor after being penetrated. It is recommended to complete more time-lapse studies and attempt to determine an average healing speed per unit volume with standard deviations. It is recommended to evaluate the MPU-IU-PDMS under exposure to radiation and atomic oxygen which it may be exposed to on an inflatable structure. An optimization process should be conducted to decrease added weight to the structure while maintaining maximum healing effectiveness over large areas of damage. It is recommended to conduct high velocity tests in a manner which will not produce a conductive carbon bi-product that will short the sensor, or manually remove a comparable amount of material to that of the damage done during hypervelocity testing to further evaluate the performance of the sensor.

6 REFERENCES

[1] de Groh, K. K., Banks, B. A., Miller, S. K. R., and Dever, J. A. Degradation of Spacecraft Materials. Elsevier Inc., 2018.

[2] Loomis, I. Tiny Micrometeorites Reveal Clues about the Solar System's Ancient Past. https://astronomy.com/magazine/news/2020/08/excavating-cosmic-fossils.

[3] Garcia, M. Orbital Debris. https://www.nasa.gov/mission_pages/station/news/orbital_debris.html.

[4] bCorbett, J., "Micrometeoroids and orbital debris (MMOD)," NASA Available: https://www.nasa.gov/centers/wstf/site_tour/remote_hypervelocity_test_laboratory/micrometeoroid_and_orbital_debris.html.

[5] Eric L., C. "Handbook for Designing MMOD Protection Astromaterials Research and Exploration Science Directorate Human Exploration Science Office NASA Johnson Space Center." 2009.

[6] "Instrumentation needs of inflatable space structures - NASA technical reports server (NTRS)," NASA Available: https://ntrs.nasa.gov/citations/20190032190.

[7] de la Fuente, H., Raboin, J. L., Spexarth, G. R., and Valle, G. D. "TransHab: NASA's Large-Scale Inflatable Spacecraft." Collection of Technical Papers - AIAA/ASME/ASCE/AHS/ASC Structures, Structural Dynamics and Materials Conference, Vol. 1, No. III, 2000, pp. 2157–2165.

[8] Valle, G., Litteken, D., and Jones, T. C. "Review of Habitable Softgoods Inflatable Design, Analysis, Testing, and Potential Space Applications." AIAA Scitech 2019 Forum, No. January, 2019, pp. 1–15

[9] "Bigelow expandable activity module (BEAM) ISS year - two - NASA technical reports server (NTRS)," NASA Available: https://ntrs.nasa.gov/citations/20180006494.

[10] Bigelow Aerospace B330. https://bigelowaerospace.com/pages/b330/.

[11] Bigelow Aerospace Technologies. https://bigelowaerospace.com/pages/our-technology/.

[12] "International Space Station." Choice Reviews Online, Vol. 53, No. 01, 2015.

[13] Anees, M., Gbaguidi, A., Kim, D., and Namilae, S. "Structural Health Monitoring of Inflatable Structures for MMOD Impacts." Nondestructive Characterization and Monitoring of Advanced Materials, Aerospace, and Civil Infrastructure 2017, Vol. 10169, No. April 2017, 2017.

[14] Dunbar, B., “Technology readiness level,” NASA Available: https://www.nasa.gov/directorates/heo/scan/engineering/technology/technology_readiness_level.

[15] Seedhouse, E. “Bigelow Expandable Activity Module.” Bigelow Aerospace, 2015, pp. 87–98.

[16] Brandon, E. J., Vozoff, M., Kolawa, E. A., Studor, G. F., Lyons, F., Keller, M. W., Beiermann, B., White, S. R., Sottos, N. R., Curry, M. A., Banks, D. L., Brocato, R., Zhou, L., Jung, S., Jackson, T. N., and Champaigne, K. “Structural Health ManagementTechnologies for Inflatable/Deployable Structures: Integrating Sensing and Self-Healing.” Acta Astronautica, Vol. 68, Nos. 7–8, 2011, pp. 883–903.

[17] Gola, Y., Kim, D., and Namilae, S. “Piezoresistive Nanocomposites for Sensing MMOD Impact Damage in Inflatable Space Structures.” Composites Communications, Vol. 21, No. August 2019, 2020.

[18] Liou, J. C., Corsaro, R., Giovane, F., Anderson, C., Sadilek, A., Burchell, M., and Hamilton, J. “DRAGONS – A Micrometeoroid and Orbital Debris Impact Sensor.” 2015, pp. 1–6.

[19] Anz-Meador, P., Ward, M., Manis, A., Nornoo, K., Dolan, B., Claunch, C., and Rivera, J. “The Space Debris Sensor Experiment.” First International Orbital Debris Conference, Vol. 3, No. 6026, 2019.

[20] “Applications of capacitors,” Capacitor Concepts Available: http://hyperphysics.phy-astr.gsu.edu/hbase/electric/capcon.html#c1

[21] “Polarization of dielectric,” Dielectrics Available: http://hyperphysics.phy-astr.gsu.edu/hbase/electric/dielec.html.

[22] Ni, N., and Zhang, L. “Dielectric Elastomer Sensors.” Elastomers, 2017.

[23] Fox, J. W., and Goulbourne, N. C., “A study on the effect of flexible electrodes and passive layers on the performance of dielectric elastomer membranes,” Aerospace, 2006.

[24] Kang, J., Son, D., Wang, G. J. N., Liu, Y., Lopez, J., Kim, Y., Oh, J. Y., Katsumata, T., Mun, J., Lee, Y., Jin, L., Tok, J. B. H., and Bao, Z. “Tough and Water-Insensitive Self-Healing Elastomer for Robust Electronic Skin.” Advanced Materials, Vol. 30, No. 13, 2018, pp. 1–8.

[25] Biggs, J., Danielmeier, K., Hitzbleck, J., Krause, J., Kridl, T., Nowak, S., Orselli, E., Quan, X., Schapeler, D., Sutherland, W., and Wagner, J., “Electroactive Polymers: Developments of and perspectives for dielectric elastomers,” Angewandte Chemie International Edition, vol. 52, 2013, pp. 9409–9421.

[26] Trung, T. Q., and Lee, N. E. “Flexible and Stretchable Physical Sensor Integrated Platforms for Wearable Human-Activity Monitoring and Personal Healthcare.” Advanced Materials, Vol. 28, No. 22, 2016, pp. 4338–4372.

[27] Kussmaul, B., Risse, S., Kofod, G., Waché, R., Wegener, M., McCarthy, D. N., Krüger, H., and Gerhard, R., “Enhancement of dielectric permittivity and electromechanical response in silicone elastomers: Molecular grafting of organic dipoles to the Macromolecular Network,” Advanced Functional Materials, vol. 21, 2011, pp. 4589–4594.

[28] Hu, W., Zhang, S. N., Niu, X., Liu, C., and Pei, Q., “An aluminum nanoparticle–acrylate copolymer nanocomposite as a dielectric elastomer with a high dielectric constant,” Journal of Materials Chemistry C, vol. 2, 2014, p. 1658.

[29] Kossi, A., Bossis, G., and Persello, J., “Electro-active elastomer composites based on doped titanium dioxide,” Journal of Materials Chemistry C, vol. 3, 2015, pp. 1546–1556.

[30] Li, Z., Haigh, A., Soutis, C., Gibson, A., and Sloan, R., “Dielectric constant of a three-dimensional woven glass fibre composite: Analysis and measurement,” Composite Structures, vol. 180, 2017, pp. 853–861.

[31] Utrera-Barrios, S., Verdejo, R., López-Manchado, M. A., and Hernández Santana, M., “Evolution of self-healing elastomers, from extrinsic to combined intrinsic mechanisms: A Review,” Materials Horizons, vol. 7, 2020, pp. 2882–2902.

[32] White, S. R., Sottos, N. R., Geubelle, P. H., Moore, J. S., Kessler, M. R., Sriram, S. R., Brown, E. N., and Viswanathan, S., “Autonomic healing of polymer composites,” Nature News Available: https://www.nature.com/articles/35057232.

[33] Guo, H., Han, Y., Zhao, W., Yang, J., and Zhang, L., “Universally autonomous self-healing elastomer with high stretchability,” Nature Communications, vol. 11, 2020.

[34] Jia, X.-Y., Mei, J.-F., Lai, J.-C., Li, C.-H., and You, X.-Z., “A highly stretchable polymer that can be thermally healed at mild temperature,” Macromolecular Rapid Communications, vol. 37, 2016, pp. 952–956.

[35] Platonova, E., Chechenov, I., Pavlov, A., Solodilov, V., Afanasyev, E., Shapagin, A., and Polezhaev, A., “Thermally remendable polyurethane network cross-linked via reversible Diels–Alder reaction,” Polymers, vol. 13, 2021, p. 1935.

[36] Xu, C., Cao, L., Lin, B., Liang, X., and Chen, Y., “Design of self-healing supramolecular rubbers by introducing Ionic cross-links into natural rubber via a controlled vulcanization,” ACS Applied Materials & Interfaces, vol. 8, 2016, pp. 17728–17737.

[37] Zhang, L., Qiu, T., Zhu, Z., Guo, L., and Li, X., “Self-healing polycaprolactone networks through thermo-induced reversible disulfide bond formation,” Macromolecular Rapid Communications, vol. 39, 2018, p. 1800121.

[38] Suriano, R., Bernasconi, R., Magagnin, L., and Levi, M., “4D printing of smart stimuli-responsive polymers,” Journal of The Electrochemical Society, vol. 166, 2019.

[39] Wei, M., Zhan, M., Yu, D., Xie, H., He, M., Yang, K., and Wang, Y., “Novel poly(tetramethylene ether)glycol and poly(ε-caprolactone) based dynamic network via quadruple hydrogen bonding with triple-shape effect and self-healing capacity,” ACS Applied Materials & Interfaces, vol. 7, 2015, pp. 2585–2596.

[40] Xie, Z., Hu, B.-L., Li, R.-W., and Zhang, Q., “Hydrogen bonding in self-healing elastomers,” ACS Omega, vol. 6, 2021, pp. 9319–9333

[41] Yan, X.; Liu, Z.; Zhang, Q.; Lopez, J.; Wang, H.; Wu, H.-C.; Niu, S.; Yan, H.; Wang, S.; Lei, T.; Li, J.; Qi, D.; Huang, P.; Huang, J.; Zhang, Y.; Wang, Y.; Li, G.; Tok, J. B.-H.; Chen, X.; Bao, Z. Quadruple H-Bonding Cross-Linked Supramolecular Polymeric Materials as Substrates for Stretchable, Antitearing, and Self-Healable Thin Film Electrodes. J. Am. Chem. Soc. 2018, 140, 5280−5289.

[42] Xu, J.; Chen, P.; Wu, J.; Hu, P.; Fu, Y.; Jiang, W.; Fu, J. Notch- Insensitive, Ultrastretchable, Efficient Self-Healing Supramolecular Polymers Constructed from Multiphase Active Hydrogen Bonds for Electronic Applications. Chem. Mater. 2019, 31, 7951−7961.

[43] Hentschel, J.; Kushner, A. M.; Ziller, J.; Guan, Z. Self-Healing Supramolecular Block Copolymers. Angew. Chem., Int. Ed. 2012, 51, 10561−10565.

[44] Liu, M.; Liu, P.; Lu, G.; Xu, Z.; Yao, X. Multiphase-Assembly of Siloxane Oligomers with Improved Mechanical Strength and Water-Enhanced Healing. Angew. Chem., Int. Ed. 2018, 57, 11242−11246.

[45] Song, Y.; Liu, Y.; Qi, T.; Li, G. L. Towards Dynamic but Supertough Healable Polymers through Biomimetic Hierarchical Hydrogen-Bonding Interactions. Angew. Chem., Int. Ed. 2018, 57, 13838−13842.

[46] Wang, H.; Liu, H.; Cao, Z.; Li, W.; Huang, X.; Zhu, Y.; Ling, F.; Xu, H.; Wu, Q.; Peng, Y.; Yang, B.; Zhang, R.; Kessler, O.; Huang, G.; Wu, J. Room-temperature autonomous self-healing glassy polymers with hyperbranched structure. Proc. Natl. Acad. Sci. U.S.A. 2020, 117, 11299−11305.

[47] Chen, H.; Koh, J. J.; Liu, M.; Li, P.; Fan, X.; Liu, S.; Yeo, J. C. C.; Tan, Y.; Tee, B. C. K.; He, C. Super Tough and Self-Healable Poly(dimethylsiloxane) Elastomer via Hydrogen Bonding Association and Its Applications as Triboelectric Nanogenerators. ACS Appl. Mater. Interfaces 2020, 12, 31975−31983.

[48] Wang, Y.; Guo, Q.; Su, G.; Cao, J.; Liu, J.; Zhang, X. Hierarchically Structured Self-Healing Actuators with Superfast Light and Magnetic-Response. Adv. Funct. Mater. 2019, 29, 1906198.

[49] Pena-Francesch, A.; Jung, H.; Demirel, M. C.; Sitti, M. Biosynthetic self-healing materials for soft machines. Nat. Mater. 2020, 19, 1230−1235.

[50] Xu, Z.; Chen, L.; Lu, L.; Du, R.; Ma, W.; Cai, Y.; An, X.; Wu, H.; Luo, Q.; Xu, Q.; Zhang, Q.; Jia, X. A Highly-Adhesive and Self- Healing Elastomer for Bio-Interfacial Electrode. Adv. Funct. Mater. 2021, 31, 2006432.

[51] Nasar, A. S., and Libni, G., "Forward and reverse reactions of N-methylaniline-blocked polyisocyanates: A clear step into double arrhenius plots and equilibrium temperature of thermally reversible reactions," *RSC Advances*, vol. 7, 2017, pp. 34149–34159.